

Snow Interception Relationships with Meteorology and Canopy Structure in a Subalpine Forest

Authors:

A. Cebulski¹ (ORCID ID - 0000-0001-7910-5056)

J.W. Pomeroy¹ (ORCID ID - 0000-0002-4782-7457)

¹Coldwater Laboratory, University of Saskatchewan, Canmore, Canada

Corresponding Author: A. Cebulski, alexcebulski@gmail.com

Abstract: Subcanopy snow accumulation models differ in how snow interception and ablation processes are represented and have uncertain applicability across diverse climates and forest types. Existing parameterizations of initial snow interception before unloading include inherently coupled accumulation and ablation processes, leading to difficulty in diagnosing processes and adding uncertainty to simulations when incorporated as canopy accumulation routines in models that already account for canopy snow ablation. This study evaluates the theory underpinning these parameterizations in-situ meteorological data, high-temporal resolution point-scale throughfall measurements, and fine-scale aerial lidar measurements of throughfall and canopy metrics collected from two subalpine forest plots in the Canadian Rockies. Contrary to existing theories, no association of canopy snow load or air temperature with interception efficiency was observed. Instead, forest structure emerged as the primary factor governing snow accumulation at the forest plot scale. A wind-driven snowfall event demonstrated that non-vertical hydrometeor trajectories significantly reduced throughfall depths across both forest plots. Prediction of interception efficiency for this event improved drastically when adjusted for hydrometeor trajectory angle based on a wind speed at one-third of the canopy height. Snow-leaf contact area showed high sensitivity to wind speed, increasing by up to 95% with a 1 m s^{-1} wind speed. The study proposes two new equations which model snow interception efficiency as a function of snow-leaf contact area adjusted for hydrometeor trajectory angle. This new parameterization successfully estimated interception efficiency for a snowfall event for the two forest plots in this study. By removing canopy snow ablation processes, this new

model should offer improved performance in prediction of sub-canopy snow accumulation when combined with canopy snow ablation parameterizations.

Keywords: snow interception, throughfall, ablation, forest, snowpack, lidar, process-based modelling

Introduction

Over half of North America's snow-covered zone is covered by forests (Kim et al., 2017), significantly impacting the accumulation and redistribution of subcanopy snowpacks and subsequent snowmelt runoff. Researchers have estimated that across the globe, 25–45% of annual snowfall may be lost to the atmosphere due to sublimation of snow intercepted in forest canopies (Essery et al., 2003). Snow intercepted in the canopy can sublimate and melt at much higher rates compared to the subcanopy snowpack (Floyd, 2012; Lundberg & Hallidin, 1994; Pomeroy et al., 1998), reducing the amount of snow available for runoff. Forest thinning efforts aimed at limiting sublimation losses and increasing snow accumulation increase snowmelt runoff but do not always commensurately increase spring streamflow (Golding & Swanson, 1978; Harpold et al., 2020; Pomeroy et al., 2012; Troendle, 1983). This may be due to increased ablation rates when forest cover is reduced, desynchronization of snowmelt, and sub-surface hydrology interactions (Ellis et al., 2013; Musselman et al., 2015; Pomeroy et al., 1997; Safa et al., 2021; Varhola et al., 2010). Vegetation structure controls the partitioning of snowfall into throughfall and interception, and thus governs the quantity of snow subject to sublimation from the canopy (Hedstrom & Pomeroy, 1998; Storck et al., 2002). The time that snow resides in the canopy and is available for high rates of sublimation depends on the rate of unloading (Hedstrom & Pomeroy, 1998; Roesch et al., 2001), canopy snowmelt (Mahat & Tarboton, 2014), and wind redistribution (Wheeler, 1987). Due to the significant impact of forest cover on snow accumulation and ablation, and the absence of monitoring network of forest snow accumulation (Rittger et al., 2020; Vionnet et al., 2021), land management, ecological conservation and water resource decisions rely on robust models of snow redistribution to estimate past, current and future subcanopy snowpacks.

Numerous field-based studies have developed methodologies to improve snow interception process understanding to better predict snow accumulation in forests. These methods, discussed in detail in Cebulski & Pomeroy (2024), include snow surveys mass balance (Hedstrom & Pomeroy, 1998), tree weighing (Hedstrom & Pomeroy, 1998; Katsushima et al., 2023; Lundberg, 1993; Satterlund & Haupt, 1967; Schmidt & Gluns, 1991; Storck et al., 2002), gamma ray attenuation (Calder, 1990), subcanopy lysimeters (Storck et al., 2002) and time-lapse imagery analysis (Floyd & Weiler, 2008; Lumbrago et al., 2022). Cebulski & Pomeroy (2024) notes the care needed in using these methods to distinguish interception from ablation processes. As a result, existing parameterizations for snow interception are sometimes coupled to ablation processes (e.g., Hedstrom & Pomeroy, 1998; Katsushima et al., 2023) and may not be compatible

when combined with additional canopy snow ablation process representations in uncalibrated models (Clark et al., 2020; Versegheghy, 2017; Wheater et al., 2022).

The coupling of ablation processes within existing snow interception models may explain the over estimation of subcanopy snow accumulation reported by Lundquist et al. (2021) and Lumbrazo et al. (2022) when combining the Hedstrom & Pomeroy (1998) routine with ablation parameterizations from different studies (e.g., Roesch et al., 2001). However, Gelfan et al. (2004) demonstrated accurate subcanopy snowpack simulations at study sites across the globe by treating the Hedstrom & Pomeroy (1998) and Storck et al. (2002) parameterizations separately while using a step-based function to choose either parameterization based on temperature. Additional observations of snow interception that minimize the inclusion of ablation processes could help determine if the theories in Hedstrom & Pomeroy (1998) and Storck et al. (2002) are valid for these measurements.

Previous studies have found differing relationships between maximum canopy snow load and air temperature (Hedstrom & Pomeroy, 1998; Storck et al., 2002). Lundquist et al. (2021) found improved subcanopy snowpack simulations when they omitted the maximum canopy snow load from Hedstrom & Pomeroy (1998), from a model otherwise linked to a complete representation of canopy snow ablation processes. This, combined with studies which have not found a maximum canopy snow load (Calder, 1990; Katsushima et al., 2023; Storck et al., 2002), and the attribution of decreased interception at higher canopy snow loads to ablation processes rather than reduced canopy structure due to branch bending alone in (Hedstrom & Pomeroy, 1998; Moeser et al., 2015; Satterlund & Haupt, 1967; Schmidt & Gluns, 1991), suggests the maximum canopy snow load may be much higher than existing models predict. This leads to uncertainty in the role of the maximum canopy snow load in snow interception and subsequent unloading. It may be beneficial to reformulate canopy snow ablation parameterizations as a function of canopy snow load rather than limiting initial interception for consistency with current rainfall interception theory for considering transitional rainfall-snowfall interception (e.g., Valante et al., 1997).

It remains uncertain how processes understanding developed at the branch and tree scale like bridging of gaps in canopy elements (Satterlund & Haupt, 1967) and branch bending (Pomeroy & Gray, 1995; Schmidt & Gluns, 1991) influence snow accumulation at the forest plot scale. Fine-scale observations of throughfall have only recently become feasible at the plot scale (Harder et al., 2020; Staines & Pomeroy, 2023), presenting an opportunity to determine how interception processes vary across differing spatial scales. Existing theory proposed by Hedstrom & Pomeroy (1998) suggests that moderate wind speeds, which result in horizontal hydrometeor trajectories, can increase snow-leaf contact area and thus increase interception efficiency at the plot scale. This association has also been shown in rainfall interception studies (i.e., Herwitz & Slye, 1995; Van Stan et al., 2011) to have a significant influence on observed throughfall of rain. Despite this importance for rainfall, this relationship proposed by Hedstrom & Pomeroy (1998), is typically not included in models (Clark et al., 2020; Mahat & Tarboton, 2014), as empirical support for this relationship is lacking. New methods developed

by Staines & Pomeroy (2023) to characterize the canopy at a high angular and spatial resolution have shown the potential to improve understanding of the relationship between snow interception and forest structure spatially and across differing trajectory angles. However, these insights have yet to be confirmed for additional study sites with more diverse forest structure and need to be incorporated into a theoretical framework appropriate for modelling forest snow accumulation in hydrological models.

The objective of this paper is to evaluate the theory underlying existing snow interception models using high spatial and temporal resolution measurements of subcanopy snow accumulation events with minimal ablation processes. These new observations are investigated to address the following research questions:

1. Are the existing theories regarding the relationship between meteorology and forest structure with snow interception supported by in-situ observations?
2. How is snow interception influenced by non-vertical hydrometeor trajectory angles over a wind-driven snowfall event?
3. To what extent can these findings inform the development of a new parameterization for snow interception?

Theory

Snow Interception

During calm snowfall periods, where ablation processes can be assumed negligible, the canopy snow load, L (kg m^{-2}) can be estimated as a mass balance:

$$\frac{dL}{dt} = q_{sf} - q_{tf} \quad (1)$$

where q_{sf} is the snowfall rate ($\text{kg m}^{-2} \text{s}^{-1}$) and q_{tf} is the throughfall rate ($\text{kg m}^{-2} \text{s}^{-1}$). This method avoids the influence of sublimation losses or drip from weighed tree lysimeters.

Interception efficiency, $\frac{I}{P}$ (-), which is the fraction of snow intercepted over Δt was calculated as:

$$\frac{I}{P} = \frac{\frac{dL}{dt}}{q_{sf}} \quad (2)$$

Throughfall, q_{tf} was be calculated as:

$$q_{tf} = \left(1 - \frac{I}{P}\right) \cdot q_{sf} \quad (3)$$

Hydrometeor Trajectory Angle

The trajectory angle, θ_h of a hydrometeor as the departure in degrees ($^\circ$) from a vertical plane (i.e., 0° for vertical snowfall), is shown in Herwitz & Slye (1995) to be calculated as:

$$\theta_h = \arctan \left(\frac{x_h(u_z)}{v_h(D_h)} \right) * \frac{180}{\pi} \quad (4)$$

where $v_h(D_h)$ is the terminal fall velocity of the hydrometeor (m s^{-1}), which is a function of the hydrometeor diameter, D_h and $x_h(u_z)$ is the horizontal change in the hydrometeor (m s^{-1}) which is a function within canopy wind speed, u_z at height above ground, z .

Figure 1 shows the increase in simulated θ_h calculated using Equation 4 with differing hydrometeor terminal fall velocities of 0.5, 1, and 1.5 m s^{-1} and a horizontal velocity equal to wind speed ranging from 0-20 m s^{-1} .

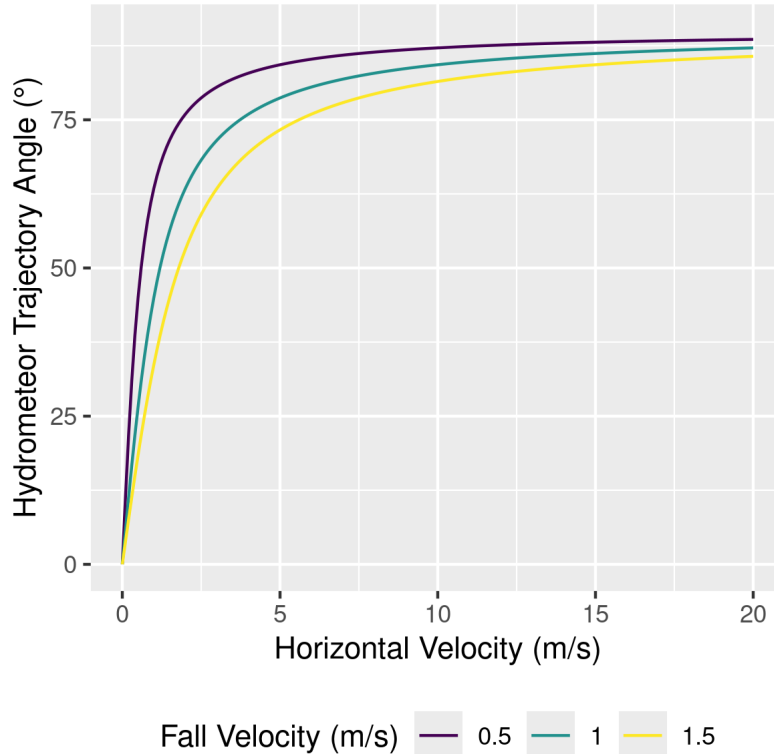


Figure 1: Plot showing the relationship of simulated hydrometeor trajectory angle (departure from zenith) with increasing horizontal velocity from Equation 4. The three different lines represent fall velocities of 0.5 m s^{-1} (purple), 1 m s^{-1} (green), 1.5 m s^{-1} (yellow).

Data and Methods

Study Site

This study was conducted at Fortress Mountain Research Basin (FMRB), Alberta, Canada, -115° W, 51° N, a continental headwater basin situated within the Canadian Rocky Mountains (Figure 2). Data from this study was collected between October 2021 and July 2023 within and surrounding two forest plots adjacent to the FMRB Powerline Station (PWL) and Forest Tower Station (FT) at ~2100 m asl. (Figure 2). The average annual precipitation at PWL Station from 2013 to 2023 was 1045 mm, with the peak annual snow water equivalent (SWE) reaching 465 kg m⁻², typically occurring in late April. The PWL and FT forest plots include discontinuous stands of 70% subalpine fir (*Abies lasiocarpa*) and 30% Engelmann spruce (*Picea engelmannii*) (Langs et al., 2020). The PWL plot is located 120 m to the northwest of FT station and contains a forest clearing with a diameter of ~12 m and is surrounded by a more closed canopy. The canopy coverage of the PWL and FT forest plots is 0.51 and 0.29 respectively. The average height of the canopy surrounding the plot to the east of the PWL station is 10.51 m and surrounding the forest plot around the FT Station is 7.12 m. The forest of the FT plot is characterized by discontinuous canopy without artificial clearings. In August of 1936 the majority of vegetation in FMRB burned during a large forest fire that affected most of the Kananaskis Valley (Fryer & Johnson, 1988). Following the fire, the forest within the the PWL and FT forest plots has naturally regenerated, though some trees have been removed for road clearing and creation of a snow study plot.

Meteorological Measurements

Measurements of air temperature and relative humidity (Vaisala model HMP155A), wind speed and direction (RM Young model 86000 2-D ultrasonic anemometer) were made 4.3 m above the ground at FT station (Figure 2). Wind speed measurements from a 3-cup anemometer (Met One model 014A), installed adjacent to the 2-D ultrasonic anemometer at 4.3 m, were used for gap filling wind speed. Additional wind speed measurements were collected by two 3-D sonic anemometers (Campbell Scientific CSAT3) installed at at 2 m (raised to 3 m February 2022) and 13.5 m above the ground at FT station. Average wind speeds at these three heights at FT station were found to follow a logarithmic relationship and a wind profile was fit using the following equation:

$$\bar{u} = \frac{u_*}{K} \ln\left(\frac{z - d_0}{z_0}\right) \quad (5)$$

where \bar{u} is average wind speed, u_* is the friction velocity (m s⁻¹), z is the height above ground (m), d_0 is the displacement height (m), z_0 is the roughness length of momentum (m), and k is the von Kármán Constant (-).

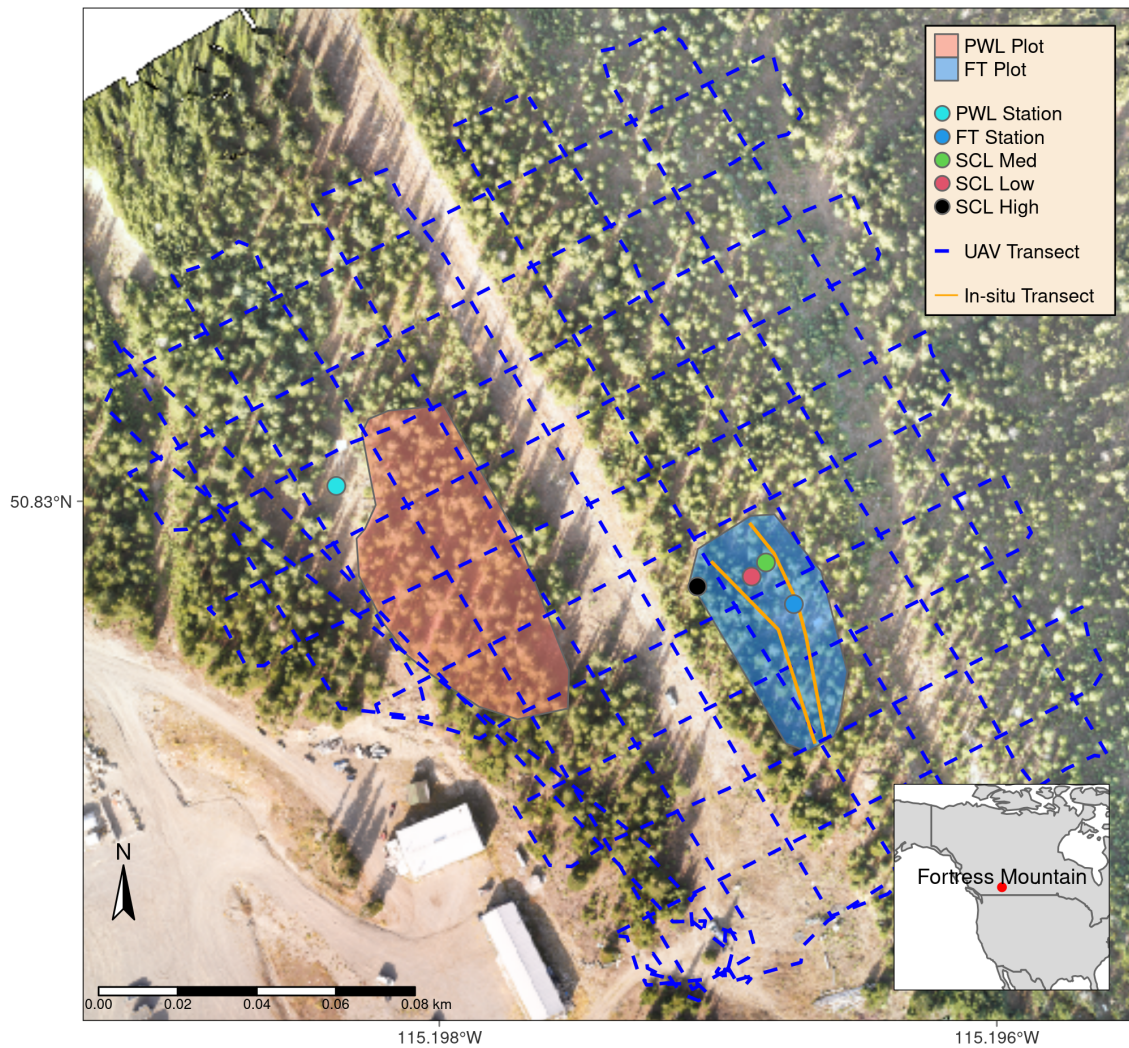


Figure 2: Map showing the location of forest plots, flux towers, SCL instruments and survey transects. Inset map on the lower right shows the regional location of Fortress Mountain Research basin.

To determine the displacement height and roughness length parameters, an optimization function “optim” from the stats R package (R Core Team, 2024) was used that minimized the squared error between modelled and observed wind speeds. The parameters for the wind speed profile include a roughness length of 0.50 m, displacement height of 0.58m. At PWL station, the snowfall rate was measured by an Alter-shielded OTT Pluvio weighing precipitation gauge 2.6 m above ground, corrected for undercatch following phase correction by Harder & Pomeroy (2013) and catch efficiency by Smith (2007). Wind speed for undercatch correction was measured by a 3-cup anemometer (Met One model 014A) at a height of 2.6 m at PWL station. An optical disdrometer (OTT Parsivel2) provided measurements of hydrometeor particle size and vertical velocity. All measurements were recorded at 15-min intervals using Campbell Scientific Canada dataloggers, except the Parsivel2 which was recorded at 1-minute intervals by an onsite computer.

Lysimeter Data

Three subcanopy lysimeters (SCLs) were installed surrounding FT Station Figure 2 to provide 15-minute interval measurements of sub-canopy snowfall. Figure 3 shows the three SCLs which consisted of a plastic horse-watering trough with an opening of 0.9 m^2 and depth of 20 cm suspended from a load cell (Intertechnology 9363-D3-75-20T1) attached to an aluminum pipe connected between two trees. For 26 distinct snowfall events, where canopy snow ablation rates were deemed negligible, the throughfall rate, q_{tf} , was calculated by dividing the load cell weight by the cross-sectional area of the SCL opening and calculating the rate of change at 15-minute intervals. Interception efficiency was quantified at the same 15-minute intervals during these events using Equation 1 and Equation 2, incorporating measurements of q_{tf} from the SCLs and q_{sf} from the PWL snowfall gauge. Timelapse imagery, mass change on a weighed tree lysimeter “hanging tree” and in-situ observations were used to ensure the ablation of snow intercepted in the canopy or snow on the ground was minimal over each of the selected snowfall events. The canopy structure surrounding three SCLs is shown in Figure 3 and was measured using hemispherical photography (Nikon Coolpix 4500 and EC-F8 hemispherical lens) and the hemispheR R package Chianucci & Macek (2023). The leaf area index and canopy coverage from hemispherical photo analysis is shown in Table 1.

Table 1: Canopy structure of the three subcanopy lysimeters (SCL) located proximal to the FT Station. Leaf area index (LAI) and Canopy Coverage was measured using hemispherical photo analysis with the R package hemispheR.

| Name | LAI (-) | Canopy Coverage (-) |
|--------|---------|---------------------|
| Sparse | 1.59 | 0.73 |
| Mixed | 1.86 | 0.78 |
| Closed | 2.11 | 0.82 |

The weighed tree lysimeter, measured the weight of canopy snow load, L_{wt} (kg). A live subalpine fir (*Abies lasiocarpa*) tree was cut and suspended from a load cell (Artech S-Type 20210-100) each year to record the weight of the tree. The bottom of the tree was sealed with pruning tar to restrict sap loss. The base of the tree was attached to a support system that allows for vertical movement but limited abrupt horizontal movements and prevented spinning. The weight of snow intercepted on the weighed tree was scaled to an areal estimate of canopy snow load (L , kg m⁻²) using measurements of areal throughfall (kg m⁻²) from manual snow surveys and snowfall from the PWL Station snowfall gauge (see description of method in Hedstrom & Pomeroy, 1998). While not used in the computation of interception efficiency, the weighed tree provided a continuous measurement of L which were used to filter out periods of canopy snow ablation identified by periods of time that exhibited a loss in L .

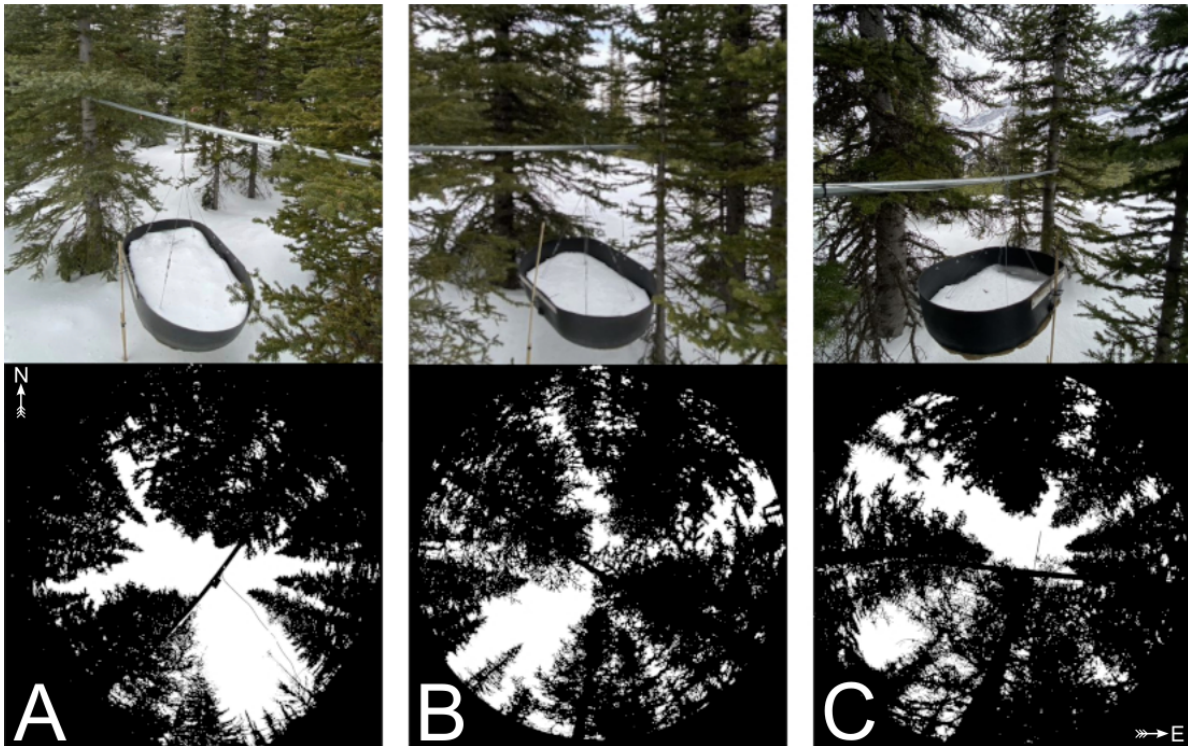


Figure 3: Images of the three subcanopy lysimeters (SCL) and surrounding canopy located in sparse (A), mixed (B), and dense (C) canopy. The top row presents a side view of each SCL and the bottom row shows hemispherical photographs classified using the hemispheR R package. These hemispherical images are oriented with north at the top and have been flipped to provide a view from above (i.e., east is on the right side of each image).

UAV-Lidar Data Collection Processing

Two uncrewed aerial vehicle (UAV) lidar surveys were conducted before and after a 24 hour snowfall event that occurred between March 13th and March 14th, 2023 to facilitate the measurement of snow accumulation and canopy structure metrics. The UAV (FreeFly Alta X) was equipped with a REIGL miniVUX-2 airborne laser scanner payload, an Applanix APX-20 inertial measurement unit (IMU) and global navigation satellite system (GNSS). The UAV was flown 90 m above the ground at a speed of 3 m s^{-1} following a preprogrammed flight trajectory shown in Figure 2. A detailed description of the UAV and payload sensor specifications and flight settings is provided in the supporting information section. Methods outlined by Harder et al. (2020) and Staines & Pomeroy (2023) were incorporated to reconcile survey lidar, IMU and GNSS data. A vertical offset of up to 6 cm between UAV-lidar flight lines was observed in the resulting point clouds on March 13th and 14th, 2024 and was attributed to IMU position drift. This offset between flight lines was corrected using the BayesStripAlign software v2.24 (BayesMap Solutions, 2024). After strip alignment, the mean elevation bias (lidar minus GCP) was 0.000 m and the RMS error changed from 0.055 m to 0.038 m March 13th and changed from 0.033 m to 0.029 m on March 14th. The point cloud density ranged from ~1200 returns m^2 in open clearings to ~2200 m^2 in sparse forest for both the March 13 and 14th surveys after all flight paths were combined. Quality control, ground classification and calculation of the change in between two UAV-lidar point clouds was conducted using the LAStools software package (LAStools, 2024). More details on the UAV-lidar processing workflow are provided in the supporting information.

Snow Surveys

In-situ Snow Depth and Density

In-situ fresh snow surveys provided measurements of subcanopy throughfall depth and density following the transects shown in Figure 2. Twelve fresh snow surveys (six pre- and post-snowfall event pairs) at 30 locations were selected which had minimal ablation and redistribution between pre and post surveys and were used to scale the weighed tree following methods outline in Hedstrom & Pomeroy (1998). When conditions allowed for a UAV-lidar flight, the in-situ snow surveys were conducted following the UAV-lidar flight to assess the accuracy of the throughfall measurements and provide a fresh snow density for the calculation of SWE (kg m^{-2}). A 1000 cm^3 snow density wedge sampler (RIP Cutter, <https://snowmetrics.com/shop/rip-1-cutter-1000-cc/>) was used to measure the density of the fresh snow layer, $\overline{\rho_{tf}}$ (kg m^{-3}) from snow pits. The throughfall depth measurements, ΔHS were converted to SWE using the following equation:

$$\Delta SWE_{tf} = \Delta HS \cdot \overline{\rho_{tf}} \quad (6)$$

Differential GNSS rover coordinates, with ± 2.5 cm 3D uncertainty, were taken at each snow sampling location so the locations could be queried later from the UAV-lidar rasters. If a pre-event crust layer was present the depth of post event fresh snow accumulation above the crust layer were interpreted as throughfall over the event. In the absence of a defined crust layer, the difference in pre- and post-event snow depth to ground was interpreted as event throughfall.

UAV-Lidar Snow Depth

Two UAV-lidar surveys, one prior to a snowfall event on March 13, 2023 at 10:00 CST and another following snowfall on March 14, 2023 at 11:00 CST enabled fine-scale analysis of snow accumulation and canopy structure within the FT and PWL forest plots. This period was selected based on two criteria: 1) it provided sufficient cumulative snowfall to result in a low relative error in UAV-LiDAR measured throughfall, and (2) minimal redistribution and ablation was observed, as confirmed by the SCLs, weighed tree, and time-lapse imagery. The change in elevation between the two UAV-lidar surveys was interpreted as the increase in snow accumulation, ΔHS over the snowfall event. Further details on the generation of 25 cm horizontal resolution ΔHS rasters from the UAV-lidar point clouds is provided in the supporting information.

UAV-Lidar Canopy Metrics

To characterize the canopy structure, the voxel ray sampling (VoxRS) methodology for lidar data analysis was employed, as developed by Staines & Pomeroy (2023), for both UAV-lidar surveys. This method was chosen for its ability to provide canopy metrics that are less sensitive to the inherent non-uniform nature of lidar sampling data, which often results from beam occlusion in vegetation and leads to reduced points near the ground. The VoxRS algorithm is publicly available at <https://github.com/jstaines/VoxRS>. The canopy products produced from VoxRS here include: canopy contact number, the mean theoretical number of canopy contacts for a given ray, and radiation transmittance (τ) all with units (-). See supporting information in Staines & Pomeroy (2023) for details on how these metrics are computed. The fraction of snow-leaf contact area per unit area of ground used in Hedstrom & Pomeroy (1998), and hereafter called leaf contact area (C_p), was calculated as:

$$C_p(C_c, \theta_h, L) = 1 - \tau \quad (7)$$

$$C_p(C_c, \theta_h, L) = \begin{cases} 1 - \tau, & \text{if } \theta_h > 0^\circ \\ 1 - \tau \approx C_c, & \theta_h = 0^\circ \end{cases} \quad (8)$$

where C_p is a function of the canopy coverage C_c , θ_h and L . C_p is approximately equal to canopy coverage (C_c) for vertical snowfall trajectories. However, for non-vertical snowfall $1 > C_p > C_c$.

Statistics and Regression Models

To determine how forest structure was associated with interception efficiency at different azimuth and zenith angles over the March 13-14 snowfall event, each portion of the hemisphere at each grid location was considered. The relationship between interception efficiency and canopy contact number was found to be linear and thus the Pearson Correlation Coefficient, ρ_p was calculated using the ‘stats’ package in R (R Core Team, 2024) to quantify the association between a single raster of interception efficiency and the 32,760 rasters containing the canopy contact number hemisphere for each portion of the hemisphere (azimuth [0°, 1°, ..., 359°], zenith angle [0°, 1°, ..., 90°]) for each of the 25 cm grid cells across the FT and PWL forest plots.

Linear and non-linear regression models were developed to assess relationships in the observed data. Linear models were fitted using ordinary least squares regression via the ‘lm’ function from the R ‘stats’ package (R Core Team, 2024) to analyze two relationships: (1) between interception efficiency and meteorological variables and (2) between interception efficiency and leaf contact area. The later was forced through the origin based on the theoretical justification that the dependent variable should be zero when the independent variable is zero. Kozak & Kozak (1995) noted, the default R^2 value provided for least squares models forced through the origin by many statistical packages can be misleading. Therefore, these R^2 values were adjusted using Equation 10 in Kozak & Kozak (1995). Non-linear models were fitted using non-linear least squares (nls) regression via the ‘nls’ function in ‘stats’ package in R.

Results

The influence of meteorology on snow interception

Figure 4 plots canopy snow load against cumulative snowfall over 26 snowfall events using the three SCLs and the PWL snowfall gauge. The duration and meteorology of each snowfall event is summarized in Table 2 and shows air temperature over these periods ranged from a minimum of -24.48 to a maximum of -24.48°C. Wind speeds ranged from a minimum of 0.03 to a maximum of 0.03. Canopy snow load was observed in Figure 4 to increase linearly with increasing snowfall without evidence of reaching a maximum. Variation in the slope of each line in Figure 4, is attributed to differences in the meteorology and antecedent canopy snow load within and between the individual events. Variations in the canopy structure surrounding the SCL instruments as shown in Table 1, also contributed to the difference in slope. The absence

of canopy snow load measurements in Figure 4 for certain troughs during specific events was caused by damage to the subcanopy lysimeter wiring due to animals and heavy snow loads.

Figure 5 shows mean event air temperature had a weak negative association ($p < 0.05$) with mean event interception efficiency, while the other two troughs displayed insignificant relationships ($p > 0.05$). Cumulative event snowfall had a consistent negative association with cumulative snowfall, however the relationships were insignificant for all three troughs ($p > 0.05$). Event mean wind speed exhibited a relatively strong positive association with interception efficiency for the sparse ($p > 0.05$) and closed ($p < 0.05$) SCLs. A negative insignificant association was observed for the mixed SCL ($p > 0.05$). The opposing relationship of wind speed and interception efficiency between the SCLs can be explained as the mixed SCL has an opening in the canopy Figure 3, that matches the prevailing wind direction shown in Figure 7, thus increasing the amount snowfall entering the sub-canopy during increased winds. For the closed and sparse SCLs this increase in interception efficiency is interpreted to be due to an associated increase in canopy contact area as hydrometeor trajectory becomes more horizontal with increasing wind speed.

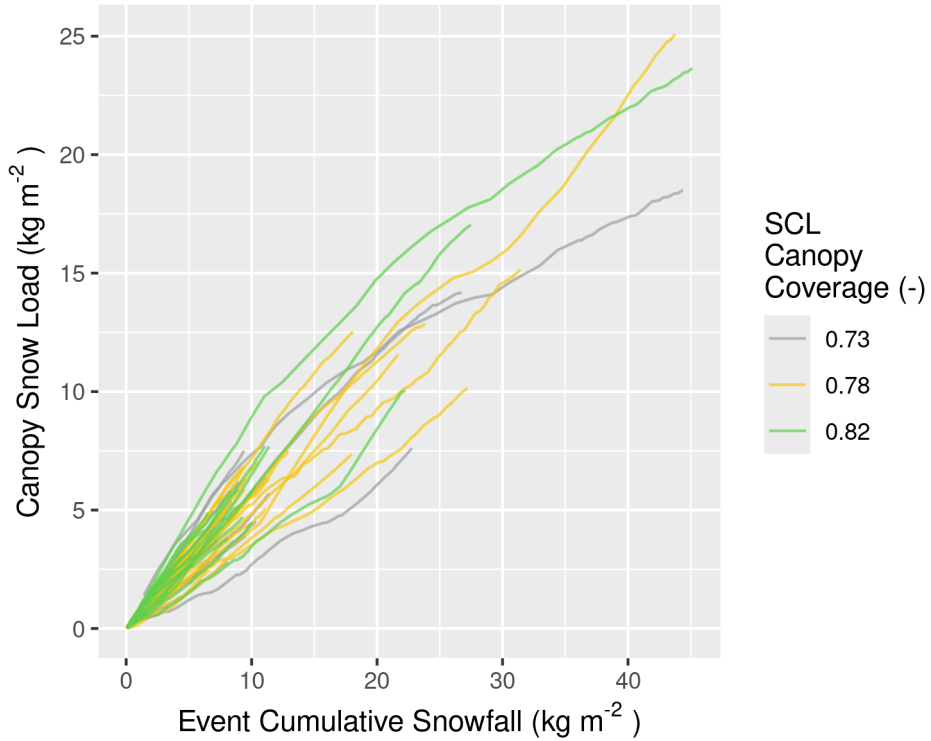


Figure 4: Plot showing the cumulative event snowfall versus the corresponding state of canopy snow load calculated using the SCLs for each of the 26 snowfall events. The SCLs are denoted by a distinct colour (grey, yellow, and green), correspond to varying canopy coverage (0.73, 0.78, and 0.82, respectively).

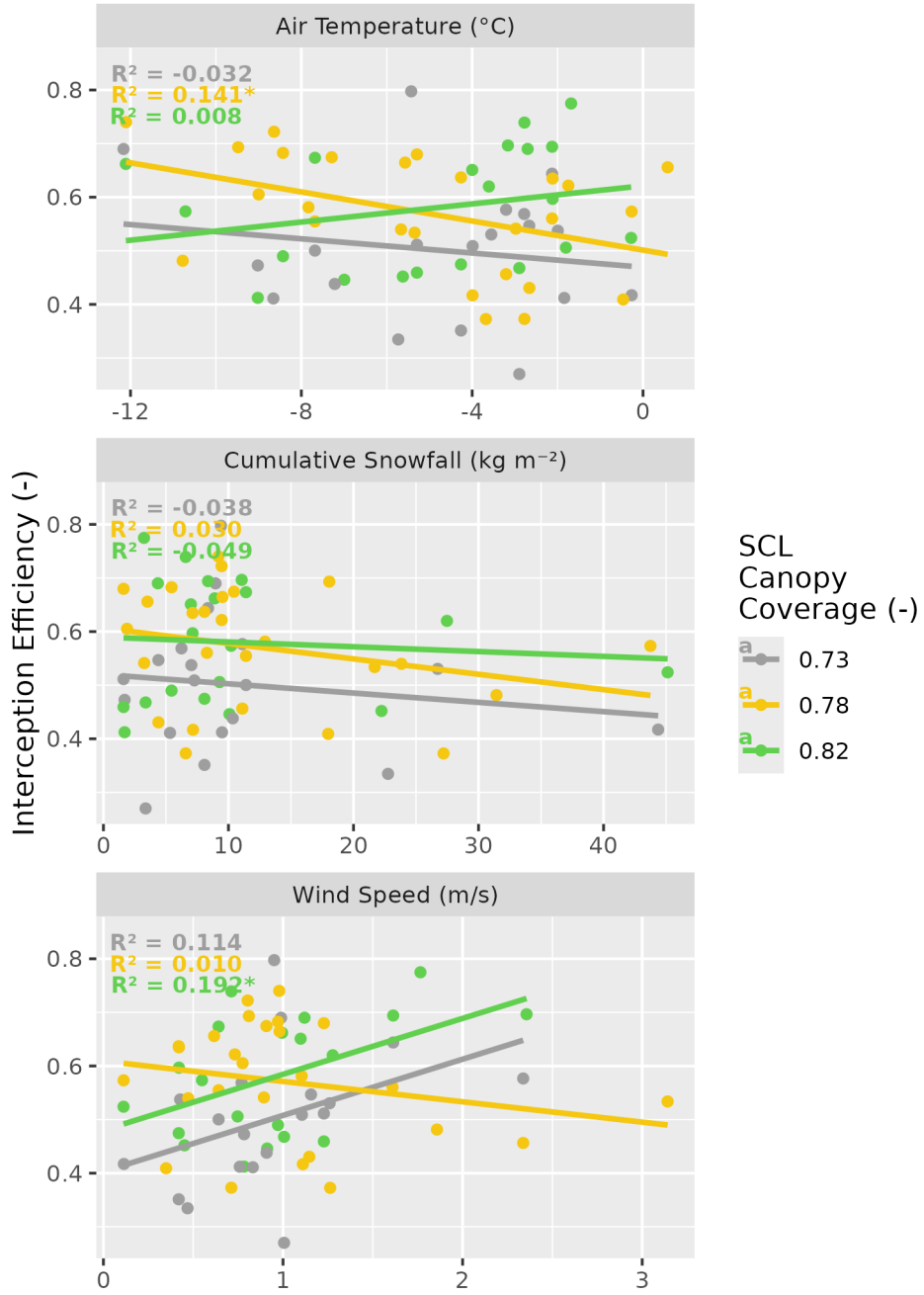


Figure 5: Scatter plots showing the mean air temperature and wind speed and total cumulative snowfall versus the mean interception efficiency measured by the SCLs for each of the 26 snowfall events. The SCLs are denoted by a distinct colour (grey, yellow, and green), correspond to varying canopy coverage (0.73, 0.78, and 0.82, respectively). A linear regression line fit to the data is shown by the solid coloured lines and the corresponding adjusted r squared value. Significant relationships ($p < 0.05$) are marked by an asterisk beside the R^2 value.

Table 2: Meteorological statistics for the 26 snowfall events.

| Start Date | Duration (Hrs) | Air Temperature (°C) | | | Wind Speed (m/s) | | | Interception Efficiency (-) | | | Total Snowfall (mm) |
|------------|-------------------|-------------------------|-------|------|------------------|------|-----|--------------------------------|------|-----|---------------------------|
| | | Min | Mean | Max | Min | Mean | Max | Min | Mean | Max | |
| 2021-12-23 | 14.50 | -6.2 | -5.3 | -4.6 | 0.6 | 3.1 | 4.6 | 0.7 | 0.8 | 1.0 | 21.7 |
| 2022-01-02 | 145.00 | -15.9 | -10.6 | -5.8 | 0.2 | 1.9 | 4.2 | 0.1 | 0.7 | 1.0 | 32.9 |
| 2022-01-17 | 11.50 | -14.8 | -7.8 | -0.8 | 0.2 | 1.1 | 1.8 | 0.0 | 0.6 | 1.0 | 12.9 |
| 2022-01-31 | 25.75 | -24.5 | -12.1 | -6.4 | 0.1 | 1.0 | 1.7 | 0.2 | 0.7 | 1.0 | 9.1 |
| 2022-02-14 | 2.25 | -9.9 | -9.0 | -8.5 | 0.4 | 0.8 | 1.2 | 0.2 | 0.5 | 0.8 | 1.7 |
| 2022-02-19 | 8.25 | -4.7 | -3.2 | -2.5 | 1.3 | 2.3 | 3.6 | 0.3 | 0.6 | 0.9 | 11.1 |
| 2022-03-01 | 54.75 | -8.3 | -5.4 | -1.0 | 0.1 | 1.0 | 3.1 | 0.4 | 0.8 | 1.0 | 9.9 |
| 2022-03-07 | 10.25 | -12.5 | -8.6 | -4.4 | 0.3 | 0.8 | 1.7 | 0.3 | 0.7 | 1.0 | 9.5 |
| 2022-03-14 | 29.25 | -2.7 | -2.1 | -0.8 | 1.0 | 1.6 | 2.9 | 0.2 | 0.6 | 0.9 | 8.4 |
| 2022-03-19 | 2.75 | -3.1 | -2.8 | -2.5 | 0.0 | 0.7 | 1.3 | 0.3 | 0.5 | 0.6 | 6.6 |
| 2022-03-23 | 6.00 | -7.9 | -5.3 | -0.9 | 0.8 | 1.2 | 1.8 | 0.4 | 0.6 | 0.9 | 1.6 |
| 2022-04-04 | 1.75 | -3.5 | -2.9 | -2.1 | 0.6 | 1.0 | 1.9 | 0.0 | 0.4 | 0.6 | 3.4 |
| 2022-04-18 | 14.50 | -5.2 | -4.0 | -2.7 | 0.4 | 1.1 | 1.9 | 0.1 | 0.5 | 0.9 | 7.4 |
| 2022-04-22 | 18.75 | -2.8 | -1.8 | -0.5 | 0.4 | 0.8 | 1.2 | 0.1 | 0.5 | 1.0 | 9.8 |
| 2022-05-09 | 5.00 | -4.9 | -4.3 | -3.2 | 0.1 | 0.4 | 0.9 | 0.2 | 0.5 | 0.9 | 8.1 |
| 2022-05-19 | 19.25 | -4.9 | -2.1 | 0.3 | 0.1 | 0.4 | 0.9 | 0.2 | 0.6 | 0.9 | 7.1 |
| 2022-06-13 | 15.00 | -1.1 | -0.3 | 0.6 | 0.1 | 0.1 | 0.4 | 0.0 | 0.5 | 0.9 | 45.3 |
| 2022-12-27 | 7.00 | -3.0 | -2.7 | -1.9 | 0.6 | 1.1 | 1.8 | 0.2 | 0.5 | 0.9 | 4.5 |
| 2023-01-27 | 16.00 | -11.5 | -7.3 | -4.5 | 0.6 | 0.9 | 1.2 | 0.1 | 0.5 | 0.8 | 10.4 |
| 2023-02-19 | 31.00 | -14.3 | -9.5 | -6.3 | 0.2 | 0.8 | 1.4 | 0.2 | 0.7 | 1.0 | 18.1 |
| 2023-02-26 | 2.00 | -9.2 | -8.4 | -6.6 | 0.2 | 1.0 | 2.1 | 0.3 | 0.5 | 1.0 | 5.4 |
| 2023-03-13 | 21.00 | -8.9 | -3.6 | -0.1 | 0.3 | 1.3 | 2.2 | 0.0 | 0.5 | 1.0 | 27.4 |
| 2023-03-24 | 15.50 | -7.9 | -5.7 | -3.5 | 0.1 | 0.5 | 1.2 | 0.1 | 0.4 | 0.7 | 23.8 |
| 2023-04-01 | 13.00 | -8.9 | -7.7 | -4.7 | 0.1 | 0.6 | 1.4 | 0.4 | 0.6 | 0.8 | 11.4 |
| 2023-04-10 | 8.25 | -1.1 | -0.5 | 0.3 | 0.1 | 0.3 | 1.0 | 0.2 | 0.4 | 0.6 | 18.0 |
| 2023-05-08 | 1.00 | 0.2 | 0.6 | 1.0 | 0.4 | 0.6 | 0.8 | 0.6 | 0.6 | 0.7 | 3.5 |

Figure 6 shows the association between interception efficiency measured by the three SCLs and the corresponding air temperature, wind speed, canopy snow load for the same 15-minute time interval. Panel A in Figure 6 shows that 15-minute average air temperature measurements has a very low correlation ($R^2 < 0.032$) with interception efficiency for all three SCLs with significant relationships ($p < 0.05$) only for the sparse and mixed troughs. The average interception efficiency observed within air temperature bins also does not exhibit any visual trend. However, a significantly greater median interception efficiency ($p < 0.05$) was found for air temperatures below -6 °C compared to colder air temperatures using non-parametric Wilcoxon signed rank test.

Panel B in Figure 6 shows that wind speed measured at FT Station had a slightly stronger correlation with interception efficiency with R^2 ranging between 0.04 and 0.09 ($p < 0.05$ for all three SCLs) compared to the association with air temperature. The association between wind speed and interception efficiency was observed to be positive for the sparse and closed SCLs, while the mixed SCL exhibited a negative association. The opposing trend observed for the closed and sparse SCLs compared to the mixed SCL is consistent with the trend observed in Figure 5 for the event means and is also attributed to a change in snow-leaf contact area with shifting hydrometeor trajectories as a result of changing wind speed. Between wind speed bins of 0.25 and 2.75 m s⁻¹ the mean interception efficiency increased from 0.58 to 0.66 and 0.48 to 0.61 for the closed and sparse forest SCLs respectively (Figure 6, B). The mixed SCL declined from 0.59 to 0.45 for the same range in wind speed bins. A comparison interception

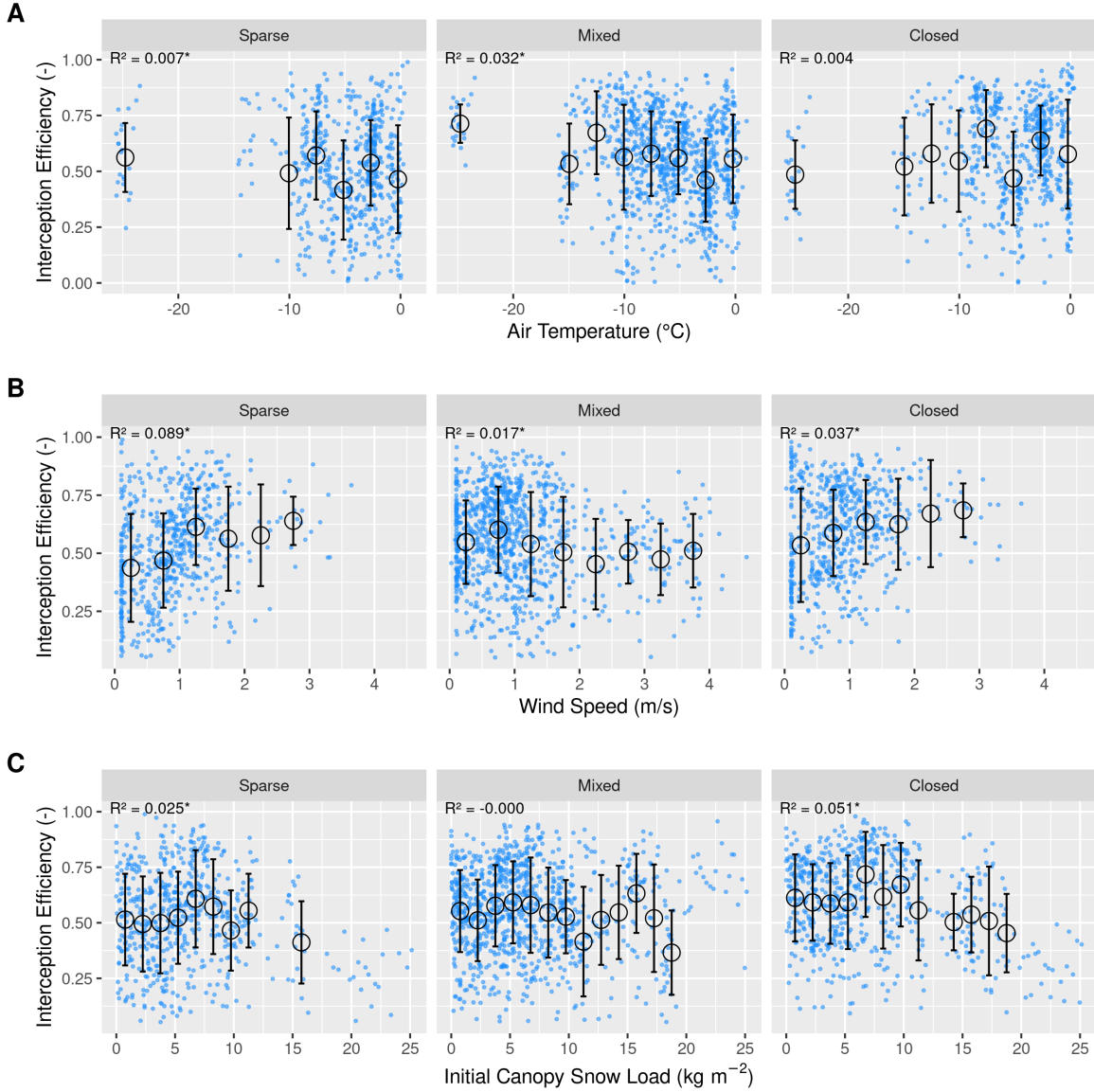


Figure 6: Scatter plots of discrete observations (blue dots) and binned data (black dots with error bars) of meteorology, canopy load, and hydrometeor characteristics versus snow interception efficiency. Panels show (A) air temperature, (B) relative humidity, (C) wind speed, (D) initial canopy snow load (the snow load observed at the beginning of the timestep), (E) hydrometeor diameter, (F) hydrometeor velocity. The black open circles show the mean of each bin and the error bars represent the standard deviations. The data were filtered to include observations with a snowfall rate $> 0 \text{ kg m}^{-2} \text{ hr}^{-1}$, throughfall rate $> 0.05 \text{ kg m}^{-2} \text{ hr}^{-1}$ to minimize noise and a snowfall rate $>$ the subcanopy lysimeter throughfall rate to minimize observations with unloading. Periods of unloading and melt were also removed through careful analysis of the weighed tree, subcanopy lysimeters, and timelapse imagery.

efficiency between low ($< 1 \text{ m s}^{-1}$) and high ($> 1 \text{ m s}^{-1}$) wind speeds by the Wilcoxon signed rank test showed that high wind speeds had significantly higher ($p < 0.05$) median interception efficiency compared to the low wind speed group for the closed and sparse SCL. Conversely, the Wilcoxon test showed the mixed SCL had significantly higher ($p < 0.05$) median interception efficiency for the low wind speed group.

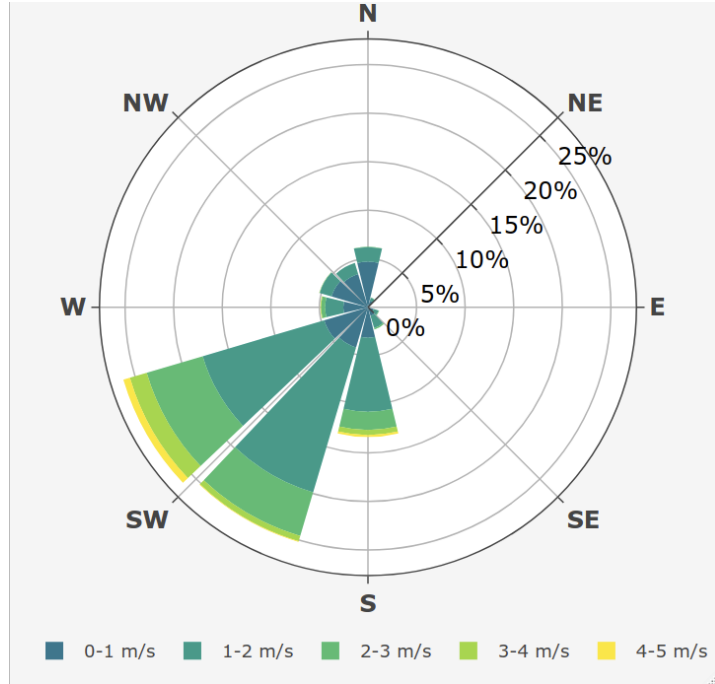


Figure 7: Wind rose showing the frequency of wind speed and direction over the 26 snowfall periods for the ultrasonic anemometer 4.3 m above ground at FT station.

Figure 6, panel C shows canopy snow load, measured at the beginning of each timestep, shows a relatively weak significant negative relationship between the 15-minute observations ($R^2 < 0.4$, $p < 0.05$) for the closed and sparse SCLs and a non-significant relationship was observed for the mixed SCL. The binned data show a small increase in interception efficiency was observed for all three troughs between canopy snow loads of 0 kg m^{-2} to 7 kg m^{-2} . This was followed by a gradual decline in interception efficiency for snow loads greater than 7 kg m^{-2} with the closed and sparse SCL (Figure 6, C). The interception efficiency measured by the mixed SCL also declines above 7 kg m^{-2} before increasing again around 16 kg m^{-2} and then declines again to a minimum interception efficiency of 0.39. A comparison of low ($< 10 \text{ kg m}^{-2}$) and high ($> 10 \text{ kg m}^{-2}$) canopy snow loads using the Wilcoxon rank-test showed the low canopy snow loads had significantly greater ($p < 0.05$) median interception efficiency compared to the high canopy snow load group. The location of the SCLs within gaps in the canopy may have contributed to these instruments registering a slight increase in interception efficiency as small branch gaps are covered by snow followed by a decline in interception efficiency as branches bend due to

the weight of snow intercepted on the branch compressing it downwards and thus reducing the canopy coverage above the SCLs.

The influence of forest structure on snow interception

UAV-lidar measurements of throughfall and canopy structure metrics provide insights on how the forest canopy influenced subcanopy snow accumulation during a wind-driven snowfall event between March 13th and 14th. This event totaled 28.7 kg m^{-2} of snowfall at PWL station and was characterized by a transition from low rates of snowfall and air temperature near 0°C to higher rates of snowfall late afternoon on March 13 coinciding with air temperatures around -2.5°C . An average wind speed of 1.27 m s^{-1} and direction of 188° was observed 4.3 m above the ground at FT Station. A logarithmic wind speed profile shown in Figure 8 provided a good fit to observed wind speeds at 2, 3, 4.3 and 13.5 m above the ground and shows the Cionco (1965) exponential function was not appropriate for the sparse canopy surrounding FT station. The friction velocity observed over the event was estimated to be 0.37 m s^{-1} by rearranging Equation 5 to solve for friction velocity using the site derived roughness length and displacement height values and incorporating the mean mean wind speed observed at FT Station at 4.3 m. The heavy snowfall over this event covered the two eddy covariance systems at FT station with snow limiting wind speed measurements to test this wind speed profile at different heights or provide a measurement of friction velocity for this event. Figure 8 shows predicted hydrometeor trajectory angles at varying heights, calculated using Equation 4 and the mean observed hydrometeor terminal velocity observed over the event of, 0.9 m s^{-1} . An average wind speed of 1.63 m s^{-1} and direction of 188° was calculated by integrating the wind speed from the surface to the mean canopy height of FT plot. The corresponding trajectory angle, calculated using Equation 4, from this integrated wind speed was 61.49° .

UAV-lidar measurements of throughfall shown in Figure 9 aligned well with 28 in-situ manual throughfall measurements with a mean bias of -0.001 m and RMSE of 0.024 m . The mean bias between these two measurements were observed to be similar within canopy gaps and within tree wells, while tree wells resulted in a larger percent bias. All three SCLs and the weighed tree registered a 2 kg m^{-2} unloading event during a brief pause in snowfall early in the morning on March 14, prior to the UAV-lidar flight. This unloading event in addition to the moderate wind speeds observed during the snowfall event likely contributed to some redistribution of snow on the ground. The relatively small unloading event compared to the amount of snow that fell during the snowfall event and minimal evidence of observed wind redistribution on the ground is inferred to have not significantly altered the UAV-lidar throughfall measurements.

Figure 9 shows the spatial distribution of throughfall and interception efficiency at the PWL and FT forest plots. Reduced throughfall and greater interception efficiency is observed on the north (lee) side of individual trees, which is interpreted to be a result of non-vertical hydrometeor trajectories caused by the steady southerly winds observed over this event. In-situ visual observations on March 13th and 14th confirmed non-vertical hydrometeor trajectories and increased canopy snow loads were observed on the windward side of individual trees. This

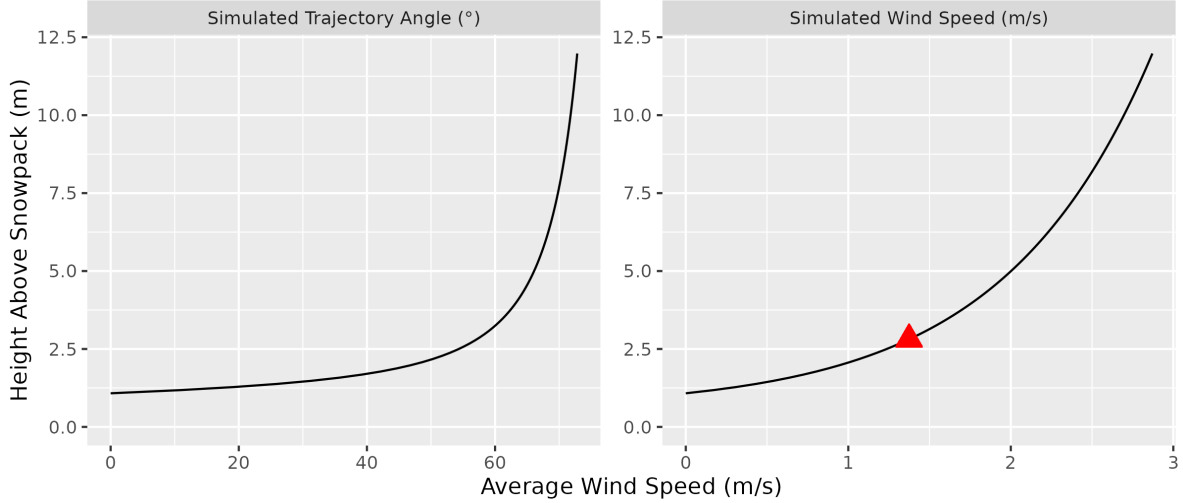


Figure 8: Wind speed profile fit to roughness length and displacement height parameters derived from anemometers at 2, 3, 4.3, and 13.5 m above ground at FT station and friction velocity observed over the March 13-14th snowfall event. The red triangle shows the mean observed wind speed at 4.3 m measured at FT station over the March 13-14 snowfall event.

effect is shown in Figure 9 to be more apparent within the PWL forest plot, compared to the FT forest plot. This may be attributed to the taller trees and higher canopy coverage within the PWL forest plot compared to the FT forest plot, where given the same trajectory angle a taller tree will produce a larger footprint.

Figure 10 presents two hemisphere plots which illustrate the correlation between C_p and interception efficiency at a 0.25 m horizontal grid cell resolution over differing azimuth and zenith angles for both the FT and PWL forest plots. These plots demonstrate a strong linear correlation between C_p and interception efficiency towards the southern portion of the hemisphere, aligning with the average event wind direction. For the PWL forest plot, the upper 97.5th percentile of the ρ_p values shown in Figure 10, were found between azimuth angles of 167° – 217°. Similarly, for the FT forest plot, the upper 97.5th percentile of ρ_p was found between azimuth angles of 171° – 223°. The zenith angle found to have the highest correlation over this azimuth range was 22° ($\rho_p = 0.7$) and 21° ($\rho_p = 0.83$) for PWL and FT respectively. The high correlation coefficients found for non-vertical zenith angles for both PWL and FT are believed to result from non-vertical hydrometeor trajectories. At near-nadir zenith angles, Figure 10 illustrates slightly lower ρ_p . In addition to the inclined hydrometeor trajectories, this may be influenced by reduced UAV-lidar returns, as shown in Figure 9, and higher percent error proximal to the trunks of individual trees due to reduced throughfall depths. However, this limitation does not significantly alter the interpretation of the results.

Figure 11 shows that the correlation between C_p and interception efficiency, resampled to a 5

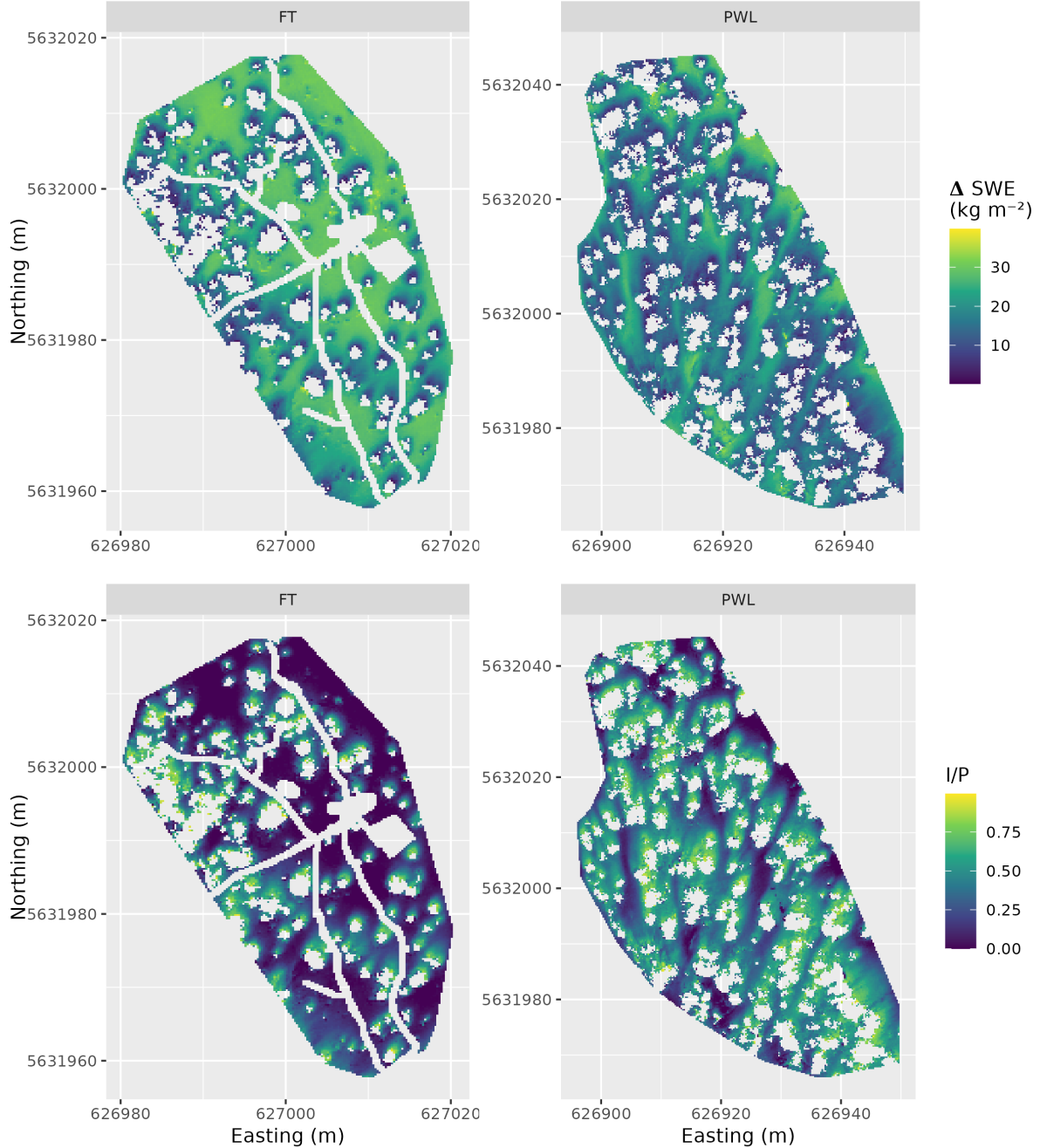


Figure 9: UAV-lidar measurements of the change in SWE (kg m^{-2}) and interception efficiency over the March 13, 2023 24 hr snowfall event for the FT and PWL forest plots at a 25 cm resolution. Transparent areas represent grids that did not have any lidar ground returns (i.e., under dense canopy proximal to tree trunks) or have been masked due to disturbance. See the location of the two forest plots within FMRB in Figure 2.

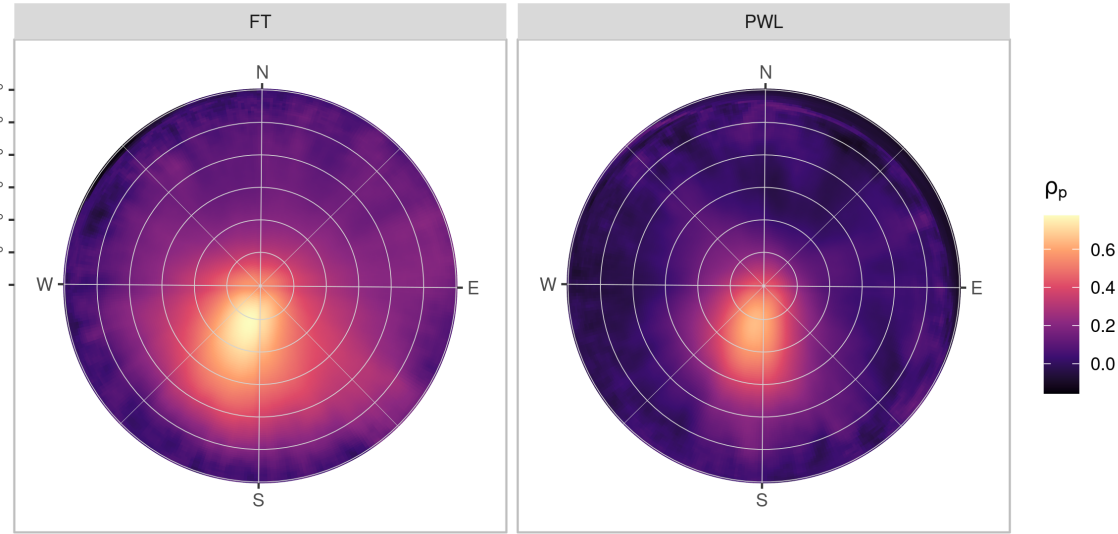


Figure 10: The Pearson Correlation Coefficient between rasters (25 cm resolution) of interception efficiency and leaf contact area for each grid cell across the study site for each azimuth angles ($0^\circ, 1^\circ, \dots, 359^\circ$) and zenith angles ($0^\circ, 1^\circ, \dots, 90^\circ$) for the FT (left) and PWL (right) forest plots.

m resolution, is stronger when C_p is adjusted for the observed shift in hydrometeor trajectory (Vector Based), compared to the nadir leaf contact angle (zenith angle of 0°). The strong association suggests that adjusted C_p is a useful predictor of interception efficiency, before ablation. For the vector-based model, adjusted C_p was calculated using the VoxRS dataset corresponding to the azimuth range and zenith angle with the highest ρ_{p} for each plot as mentioned in the previous paragraph. An ordinary least squares linear regression forced through the origin was fit to the observed data points using the following equation:

$$\frac{I}{P} = C_p(C_c, \theta_h) \cdot \alpha \quad (9)$$

where α is an efficiency constant which determines the fraction of snowflakes that contact the C_p elements and are stored in the canopy (i.e., intercepted) before canopy snow unloading or ablation processes begin.

The Nadir linear regression model provides a good overall fit to the observed data and closely follows the 1:1 line in Figure 11, with a α value of 0.95 and 0.99 for the PWL and FT plot respectively. For the PWL plot, the observed points follow a linear relationship until a C_p value of around 0.50 after which the increase in interception efficiency plateaus. After the Kozak & Kozak (1995) adjustment a negative R^2 value was determined for the PWL plot. Some of the scatter observed in the Nadir model shown in Figure 11 may be explained by grid cells which

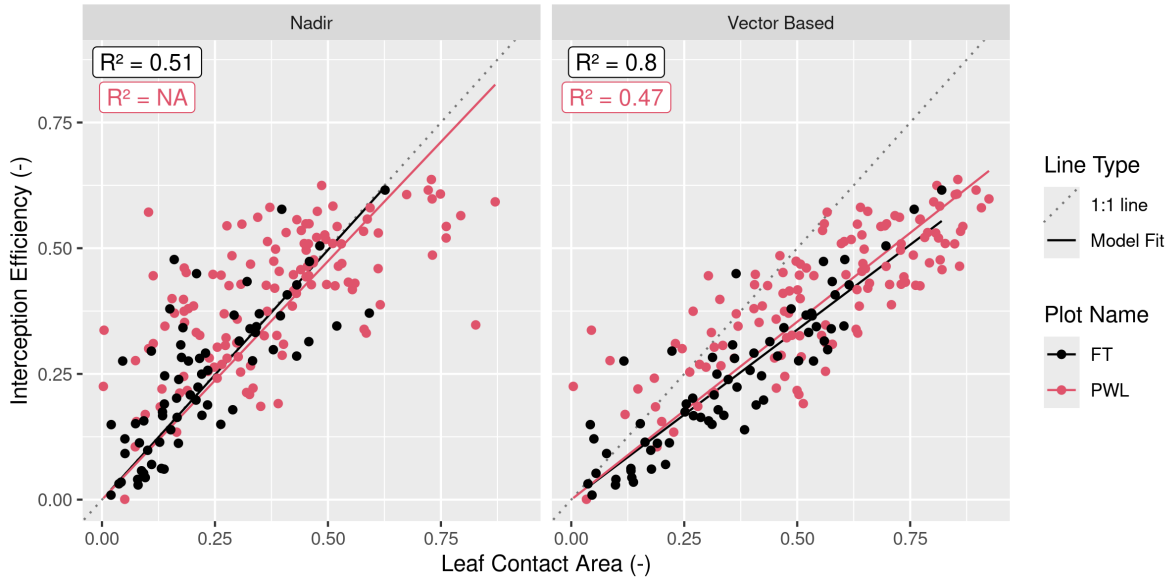


Figure 11: Scatter plots showing the relationship between leaf contact area and interception efficiency rasters resampled to a 5 m grid cell resolution. The left plot (Nadir) shows leaf contact area measured from a zenith angle of 0°. The right plot (Vector Based) shows the leaf contact area averaged over rasters with zenith angles (PWL = 22°, FT = 21°) and azimuth angles (PWL = 167°, 178°, ... 217°; FT = 171°, 172°, ... 223°). The solid lines (Model fit) show the ordinary least squares linear regression forced through the origin and fitted to the PWL (red) and FT (black) data and the light grey dotted line shows a 1:1 line. The R² values for the four different models are shown in the upper right of each panel calculated following the methods outlined in Kozak & Kozak (1995).

observed a greater interception efficiency compared to the corresponding C_c value and can be attributed to the inability of C_c to represent the increase in interception observed within canopy gaps in Figure 9. Conversely, for grid cells where interception efficiency is less than C_c , may be attributed to non-vertical trajectory hydrometeors making their way underneath the canopy as observed by the reduced interception efficiency on the windward edges of individual trees in Figure 9. This later explanation explains the non-linear relationship observed for the PWL Nadir model in Figure 9.

For the vector-based model, the relationship between interception efficiency and C_p is better represented by a linear regression model for both plots with R^2 values of 0.47 and 0.8 for PWL and FT respectively. The increase in interception efficiency with C_p follows a reduced slope compared to the Nadir models with α values of 0.71 and 0.68 for the PWL and FT plots respectively. The reduced slope for the vector-based models may be attributed to snowflakes that weaved through and/or bounced off branch elements in addition to some of the UAV-lidar measurement uncertainty which contained some unloading and redistribution. These processes would have reduced the fraction of snowfall that contacted the canopy that was intercepted.

Model error statistics are presented in Table 3 for the Nadir and vector-based models and show the vector-based model provides a better prediction of interception efficiency. The vector-based model reduced the RMSE from 0.099 to 0.062 for the FT plot and 0.146 to 0.095 for the PWL plot. The good model performance shown for the vector-based model demonstrates that using C_p adjusted for observed event hydrometeor trajectory angle has the potential to be a predictor of interception efficiency, before ablation. However, the detailed point clouds required to derived the C_p values used in this analysis are rarely available and thus more accessible methods to estimate C_p must be obtained in order to use Equation 9.

Table 3: Model error statistics provided for predictions of interception efficiency using Equation 9 and for different a values, as shown in the Model Slope column. Statistics are provided for the PWL and FT forest plots, using leaf contact area canopy metrics adjusted to zenith angles of ($0^\circ, 1^\circ, \dots, 30^\circ$) and azimuth angles ($170^\circ, 171^\circ, \dots, 220^\circ$) and nadir zenith angle of 0° . The Mean bias is the difference in the model and observed values, MAE is the mean of the absolute error, RMS Error is the root mean squared error, R^2 is the coefficient of determination adjusted using Equation 10 in Kozak & Kozak (1995).

| Plot Name | Canopy Metrics | Model Slope | Mean Bias | MAE | RMS Error | R^2 |
|-----------|----------------|-------------|-----------|-------|-----------|-------|
| FT | Nadir | 0.993 | 0.022 | 0.071 | 0.099 | 0.507 |
| FT | Vector Based | 0.676 | 0.001 | 0.047 | 0.062 | 0.804 |
| PWL | Nadir | 0.949 | 0.048 | 0.113 | 0.146 | NA |
| PWL | Vector Based | 0.707 | 0.019 | 0.078 | 0.095 | 0.469 |

The combined influence of trajectory angle and forest structure on interception

Figure 12 shows that C_p , measured from VoxRS prior to snowfall on March 13th, increases substantially with the simulated hydrometeor trajectory angle and corresponding simulated wind speed. The standard deviation in VoxRS measured C_p , illustrated by the shaded area in Figure 12 exhibits the large range in values for individual grid cells across each forest plot. Despite this large scatter, a systematic increase in the plot mean C_p results from a rise in the number of canopy elements for more horizontal portions of the hemisphere, when averaged across each forest plot, over all azimuth angles (see solid lines top row, Figure 12). The increase in C_p from C_c (i.e., $C_p - C_c$), with increasing trajectory angle is shown on the bottom row of Figure 12 and exhibits a similar relationship for both forest plots FT and PWL until trajectory angles reach approximately 60°. Beyond 60°, the PWL rate of increase slows as the C_p approaches .90 around 60°, while the FT plot, which has lower C_c , continues to rise quickly until around 75° afterwards the slope is reduced as a C_p of one is approached.

At the stand scale, increasing the hydrometeor trajectory angle results in a large rise in the VoxRS measured C_p over relatively common estimated wind speeds. For example, with a wind speed of 1 m s⁻¹ and estimated trajectory angle of 48°, the C_p increased by a fraction of 0.14 and 0.12 for the PWL and FT forest plots respectively in Figure 12 (right panel). This is a percent increase in the plot C_p from nadir of 28% and 40% for PWL and FT respectively. A similar rate of increase in C_p was observed between both the FT and PWL forest plots up to around 60° or 1.5 m s⁻¹. C_p was also quantified across trajectory angles for both PWL and FT on March 14th, post snowfall, and showed a negligible effect of canopy snow load on C_p .

A function is proposed here that calculates plot scale leaf contact area, C_p (-):

$$C_p = C_c + C_{inc}(\theta_h) \quad (10)$$

where, C_{inc} is the increase in leaf contact area from C_c which is a function of the zenith angle (hydrometeor trajectory) of interest. To estimate C_{inc} a non-linear least squares regression using a logistic function forced through the origin was fit to the VoxRS measurements at FT and PWL for simulated hydrometeor trajectory angles (see dashed lines in bottom row of Figure 12). The logistic function used predict C_{inc} as a function of θ_h is:

$$C_{inc} = \left(\frac{C_{inc}^{max}}{1 + e^{\left(\frac{\theta_0 - \theta_h}{k} \right)}} - \frac{C_{inc}^{max}}{1 + e^{\left(\frac{\theta_0}{k} \right)}} \right) \quad (11)$$

where C_{inc}^{max} is the maximum value of C_{inc} , θ_0 is the x value of the sigmoid midpoint and k is the logistic growth rate or steepness of the curve.

The resulting coefficients for LCA_{max} , θ_0 and k after the nls fit to the VoxRS dataset 0.381, 46.864 and 25.8 respectively for PWL. For FT the resulting coefficients for LCA_{max} , θ_0 and k from nls were 0.381, 46.864 and 25.8 respectively. A logistic function was selected to model

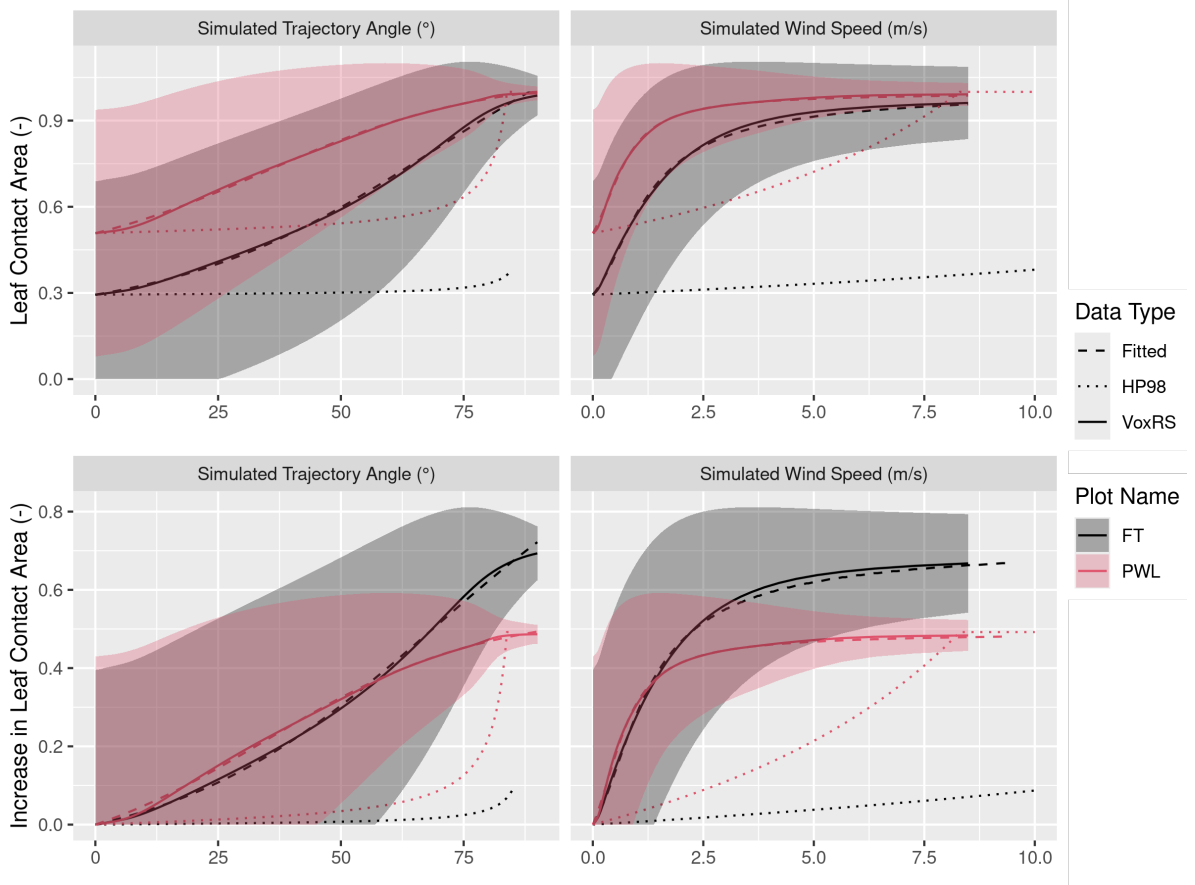


Figure 12: Plots showing the relationship between hydrometeor trajectory angle (left) and wind speed (right) with mean plot-wide snow-leaf contact area, C_p (top row) and the increase in mean plot-wide C_p , i.e., $C_p - C_c$ (bottom row). Simulated hydrometeor trajectory angle is measured as degrees from zenith. Simulated wind speed was calculated as a function of hydrometeor trajectory angle by rearranging Equation 4 and an observed event hydrometeor velocity of 0.9 m s^{-1} . The solid lines (VoxRS) represent the mean C_p (top) or increase in mean C_p (bottom) for a single zenith angle observed from VoxRS across all grid cells for each forest plot and across all azimuth angles. The shaded area represents 1 standard deviation above and below the observed VoxRS mean. The dashed lines (Fitted) represent predictions from Equation 10 (top) and Equation 11 (bottom). The dotted lines (HP98) represent the predictions from Equation 10 in Hedstrom & Pomeroy (1998). A forested downwind distance of 100 m was used for the HP98 calculation. The line colour represents the forest plot, FT (black) and PWL (red)

this relationship, as its shape was deemed most appropriate to represent the change in C_p with trajectory angle. This choice reflects the observed slow increase in C_p at near vertical trajectory angles. The logistic function also captures the non-linear increase at more horizontal trajectory angles, where snowflakes encounter more canopy area in the middle and lower section of individual trees. Additionally, the function effectively represents the gradual leveling off of C_p as it approaches full coverage (value of one).

Simulated C_p using Equation 10 is shown in the dashed lines in the top row of Figure 12 and follows closely to the VoxRS measured mean C_p . Model error statistics shown in Table 4 demonstrate that Equation 10 performed well, with a mean bias and RMSE of 0.001 and 0.0054 respectively for PWL, and -0.0004 and 0.0079 for FT. In contrast, Table 4 reveals that the Hedstrom & Pomeroy (1998) method produced significantly less accurate estimates of C_p , with a mean bias and RMSE of -0.201 and 0.233 respectively for PWL, and -0.260 and 0.324 for FT.

The use of Equation 11 requires estimates of θ_0 for a snowfall event. The estimated trajectory angle of 61.49° resulting from the mean wind speed integrated over the canopy height was much higher than the trajectory angle closer to 20° observed in Figure 10. Based on the wind speed profile in Figure 8 a trajectory angle of around 20° would have resulted from a mean wind speed of 0.36 m s^{-1} and 0.34 s^{-1} and a height above the snowpack of 1.32 m and 1.3 m for PWL and FT respectively. Based on the event average snowpack depth at FT station of 1.47 m, this corresponds to a height above the ground that is 2.79 m and 2.77 m for PWL and FT respectively and fraction of the mean canopy height of 0.27 m and 0.39 as a result of the differing tree heights within two plots. This corresponds to roughly one-third the canopy height, based on an average of the two forest plots, to achieve this low wind speed is interpreted to be a result of the conical shape of the needleleaf trees surrounding PWL and FT which have the majority of their canopy volume towards the ground. Although the wind speeds were observed to be higher near the top of the canopy, corresponding to higher trajectory angles, the reduced canopy volume at this height results in a smaller impact of these more horizontal trajectories.

Table 4: Model error statistics calculated for the prediction of leaf contact area from trajectory angle using Equation 11 (nls) and Equation 10 from Hedstrom & Pomeroy (1998) for the PWL and FT forest plots. Mean bias is the difference in the model and observed values, MAE is the mean of the absolute error, RMS Error is the root mean squared error and R^2 is the coefficient of determination. A forested downwind distance of 100 m was used for the HP98 calculation.

| Model | Plot | Mean Bias | MAE | RMS Error | R^2 |
|-------|------|-----------|--------|-----------|--------|
| HP98 | FT | -0.0991 | 0.0991 | 0.1212 | 0.7136 |
| HP98 | PWL | -0.0665 | 0.0767 | 0.0912 | 0.5045 |
| nls | FT | 0.0004 | 0.0013 | 0.0016 | 0.9997 |
| nls | PWL | 0.0006 | 0.0023 | 0.0028 | 0.9991 |

Throughfall Model Performance

The performance of Equation 9 in estimating event throughfall was assessed for the March 13-14 snowfall event at the plot scale for both FT and PWL. Event throughfall was calculated using Equation 3 with interception efficiency modelled from Equation 9 and integrating over the event time interval. The mean hydrometeor terminal velocity and total event snowfall was measured at PWL station, and wind speed was determined at height of one-third the mean canopy height using the wind speed profile in Figure 8. Additional model inputs include C_c , measured from UAV-lidar averaged over each forest plot, an α value of 1 was chosen based on the close alignment of interception efficiency and C_c to the 1:1 line in Figure 11, and the previously defined constants for Equation 11 derived for the PWL and FT plots were incorporated.

Predicted values of observed and modelled interception efficiency and ΔSWE_{tf} are shown in Table 5 along with corresponding error statistics. Figure 13 shows the vector-based model, computed using Equation 9 with C_p adjusted for estimated hydrometeor trajectory angle, closely matches UAV-lidar measurements of throughfall with a positive mean bias of 0.1 kg m^{-2} for PWL and 0.1 kg m^{-2} for FT. Figure 13 shows the nadir model, computed using Equation 9 and C_c in place of C_p , over predicted throughfall compared to the UAV-lidar measurements with a negative mean bias of -1.4 kg m^{-2} for PWL and -1.4 kg m^{-2} for FT. Table 5 shows the vector-based model has a very low absolute percent error compared to the Nadir model for PWL however for FT there is only slight improvement in absolute error. The positive bias was observed for the vector-based model was expected and is preferred compared to the nadir model as the UAV-lidar measurements of throughfall are inherently underestimates since they include some amount of unloading and redistribution. If measurements of throughfall without unloading and redistribution could have been collected it is expected the vector-based model would have further reduced error compared to the Nadir model for both FT and PWL. The improved performance of the vector-based model at PWL compared to FT, may be attributed to increased unloading and redistribution across the FT plot as a result of the sparser wind-exposed canopy.

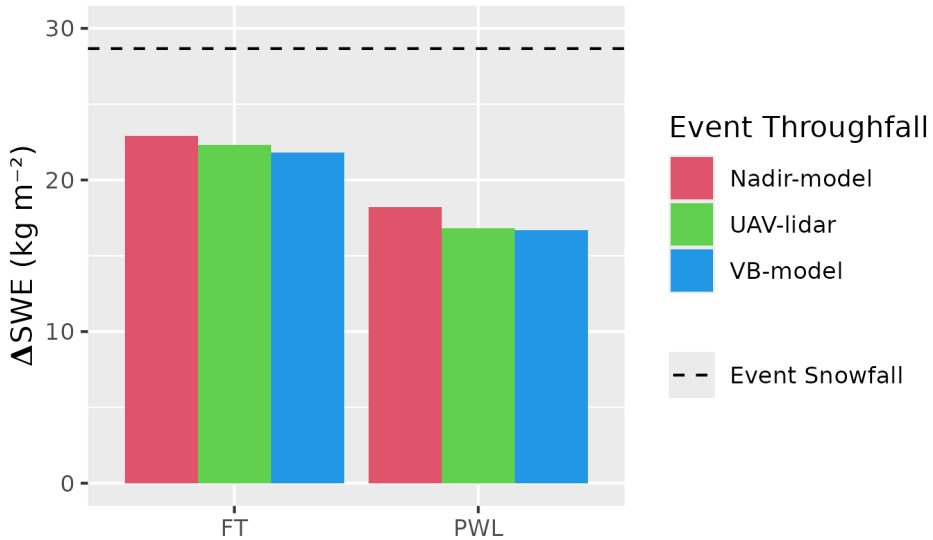


Figure 13: Bar chart comparing the observed and modelled mean change in throughfall (SWE, kg m^{-2}) over the March 13-14 snowfall event averaged over forest plots FT and PWL. The ‘nadir’ data type used Equation 9 but was not adjusted for trajectory angle and thus C_c was used instead of C_p , ‘obs’ corresponds to the UAV-lidar measured change in throughfall, and ‘VB’ is the change in throughfall predicted from the vector-based (VB) model which uses Equation 9 with C_p adjusted for trajectory angle. The black horizontal dashed line shows the accumulated SWE (kg m^{-2}) over the snowfall event to the PWL station open clearing.

Table 5: Model error statistics for model estimates of snow interception efficiency (ip) and throughfall (tf) compared to measurements of ip and tf using UAV-lidar averaged over the FT and PWL forest plots. Units for ip and tf are (-) and (kg m^{-2}) respectively. The ‘mod_type’ column refers to the method used to estimate ip and tf. The vector-based (VB) method utilized Equation 9 with C_p adjusted for trajectory angle. The nadir method also utilized Equation 9 but was not adjusted for trajectory angle and thus C_c was used instead of C_p . The obs_val column contains measurements from UAV-lidar while the mod_val column contains values from the respective mod_type method. The Mean Bias was calculated as observed minus modelled and Perc. Error is the percent error between predicted and observed values.

| plot | val_name | mod_type | obs_val | mod_val | Mean Bias | Perc. Error |
|------|----------|-------------|---------|---------|-----------|-------------|
| FT | ip | VB-model | 0.22 | 0.24 | -0.02 | -7.77 |
| FT | ip | Nadir-model | 0.22 | 0.20 | 0.02 | 9.58 |
| FT | tf | VB-model | 22.30 | 21.81 | 0.49 | 2.22 |
| FT | tf | Nadir-model | 22.30 | 22.91 | -0.61 | -2.73 |
| PWL | ip | VB-model | 0.41 | 0.42 | 0.00 | -0.85 |
| PWL | ip | Nadir-model | 0.41 | 0.37 | 0.05 | 11.72 |
| PWL | tf | VB-model | 16.81 | 16.71 | 0.10 | 0.60 |
| PWL | tf | Nadir-model | 16.81 | 18.20 | -1.39 | -8.26 |

Discussion

The point scale observations presented in this study showed air temperature had little influence on interception efficiency Figure 6 which differs from existing studies which suggested either a strong positive (Storck et al., 2002) or negative (Hedstrom & Pomeroy, 1998) relationship. An increase in initial interception efficiency before unloading was observed with increasing wind speed at two locations which were sheltered to the predominant wind direction Figure 6. This was attributed to an associated increase in C_p with wind speed. These results are consistent with observations by Schmidt & Troendle (1989) who observed a slight increase in interception with increasing wind speeds up to 6 m s^{-1} .

Compared to the influence of wind speed, interception efficiency showed a smaller sensitivity to canopy snow load at the point scale Figure 5. The slight increase in interception efficiency for smaller canopy snow loads and decline in interception efficiency for larger canopy snow loads is attributed to the influence of canopy snow load on C_p Figure 6. While small, this effect is like the theory proposed by Satterlund & Haupt (1967) that interception efficiency increases as the canopy fills with snow bridging gaps in the canopy increasing, while later declining due to branch bending and decreased canopy coverage. Hedstrom & Pomeroy (1998) and Storck et al. (2002) did not observe this initial increase, but also found declining interception efficiency at high snow loads.

The observations presented in Figure 6 and Figure 4, differ from the Satterlund & Haupt (1967), Hedstrom & Pomeroy (1998), Storck et al. (2002) and Moeser et al. (2015) theories, as canopy snow load increased linearly with snowfalls up to 45 kg m^{-2} with no evidence of approaching a maximum canopy snow load. The strong exponential decline in interception efficiency observed with increasing event snowfall in Satterlund & Haupt (1967), Hedstrom & Pomeroy (1998), Storck et al. (2002) and Moeser et al. (2015) may be a result of increased unloading rates as branches bend under heavy snow loads and hence mix ablation and interception processes to varying degrees. The low sensitivity of interception efficiency with canopy snow load found in this study may be attributed to several factors: a reduced inclusion of ablation processes in the interception efficiency measurements, limited influence of canopy snow load on C_p at this study site, and/or the compensatory effects outlined by Satterlund & Haupt (1967).

Staines & Pomeroy (2023) showed a slight increase in C_p between snow-off conditions from a single UAV-lidar scan compared to snow-on conditions derived from a combination of three UAV-lidar scans. The higher forest density in the Staines & Pomeroy (2023) study resulted in less canopy gaps and was thus not as influenced by branch bending. This may have resulted in a slightly higher influence of snow load on C_p in the Staines & Pomeroy (2023) study, compared to negligible effect reported between the March 13 and 14 UAV-lidar surveys in this study. Still, the increase in C_p resulting from snow load in Staines & Pomeroy (2023) was smaller compared to the substantial rise in C_p due to trajectory angle presented in their study and as shown in Figure 12.

Further evidence in support of canopy snow load not being directly related to interception efficiency or C_p is provided by Lundquist et al. (2021) who reported improved simulation of subcanopy snow accumulation without the use of a maximum canopy snow load when combined with ablation process representations for canopy snow melt, sublimation, wind-induced unloading and temperature induced unloading. However, Lehtonen et al. (2016) note that in northern Finland heavy canopy snow loads have been observed to continue increasing until stem breakage, under conditions favorable for the formation of significant rime-ice accretion and limited ablation. Models are available to predict the accretion of ice on tree canopies (e.g., Nock et al., 2016) however, further research is required to understand the canopy snow load required to cause stem breakage across different tree species and canopy loads.

These findings on the limited influence of air temperature and canopy snow load on initial interception challenge the theoretical basis of many existing snow interception parameterizations (Hedstrom & Pomeroy, 1998; Moeser et al., 2015; Satterlund & Haupt, 1967; Storck et al., 2002). To address this a new snow interception parameterization, Equation 9, is presented which calculates interception efficiency as a function of C_p and α . This new parameterization allows for canopy snow loading processes to be isolated from canopy snow ablation processes and is consistent with the rainfall interception literature (Valante et al., 1997). Equation 9 differs only slightly from the original Hedstrom & Pomeroy (1998) parameterization (see Equation 6 in Hedstrom & Pomeroy (1998)), in that it does not calculate interception efficiency as a function of canopy snow load and from the Storck et al. (2002) parameterization who proposed interception efficiency to be constant over time and space. The theoretical basis of

the α value in Equation 9 is that the association between C_p and interception efficiency, as shown in Figure 11, does not follow a 1:1 line as falling snow hydrometeors may bounce off the canopy elements. However, as direct measurements of C_p are not widely available, an α value of 1 is suggested if C_p is approximated from C_c using Equation 10, following the fit of the nadir model in Figure 11. The new snow interception routine is also similar to many recent rainfall interception studies, which calculate throughfall as a function of C_c (e.g., Valante et al., 1997).

Measurements of interception efficiency and canopy structure collected in this study corroborated with the Hedstrom & Pomeroy (1998) theory and showed reduced throughfall on the lee side of individual trees Figure 9. This was attributed to predominately non-vertical hydrometeor trajectory angles which can substantially increase plot-wide C_p as shown in Figure 12. It was found that the mean hydrometeor trajectory angle over a snowfall event could be predicted by using the observed hydrometeor fall velocity and a mean horizontal wind speed selected at one-third of the canopy height above the ground. A wind speed at one-third the mean canopy height is thought to be important for canopy snow accumulation as a large fraction of the horizontal cross sectional area is at this height for most needleleaf canopies. While a wind speed selected at a height higher within the canopy may have a higher speed and thus more horizontal trajectory angle, less canopy elements at this height would be available for contacting incoming hydrometeors. Katsushima et al. (2023), also proposed the wind speed at one-third the canopy height for modelling unloading of canopy snow as it corresponds to the centre of gravity when the horizontal projection of the canopy is assumed to be a triangle. However, there is uncertainty in the transferability of one-third canopy height observed here to other environments due to differing tree structures and tree species such as those with a larger trunk space or have more of their canopy contact area at higher heights above the ground (i.e., some deciduous canopies). Moreover, Equation 4 assumes a linear hydrometeor trajectory, and does not consider non-linear patterns such as wind flow wrapping around tree elements, turbulent flow, or differences in wind speed with height.

An existing method proposed in Hedstrom & Pomeroy (1998) to scale canopy coverage with wind speed failed to reproduce the observations presented in Figure 12. A new method is proposed which uses logistic function to calculate plot-wide C_{inc} as a function of θ_h and C_c . Significant scatter in VoxRS measured C_p across the two forest plots, illustrated by the high standard deviation in Figure 12, resulted from directional (azimuth) and spatial differences in canopy structure. This large scatter suggests the observed relationships in Figure 12 are only applicable at the forest stand scale where the sub metre variability C_p averages out. At this scale, Equation 11, which uses trajectory angle alone, could be sufficient to determine C_{inc} and thus C_p . Further work is required to refine the relationship proposed in Equation 11 across a range of tree species and densities. A better understanding of this relationship is also important for representing the change in light transmittance through the canopy with solar zenith angle (Niu & Yang, 2004). Also ref Dai et al. (2019) who propose a way to represent subgrid variability and gap distribution in the canopy, important for them for subcanopy turbulence.

Although the performance improvement in the vector-based model compared to the Nadir model is relatively small the positive bias of the VB model is preferred due to uncertainties with the throughfall measurements. Throughfall measurements by UAV-lidar over the snowfall event are inherently overestimates due to some unloading and redistribution of snow, which were estimated to be about 2 kg m^{-2} . Throughfall measurements that do not include unloading and redistribution would have been slightly lower and thus better matched the vector-based model. Conversely, the Nadir model which has a stronger negative bias, would result in further overestimates. Although the Nadir model provided good performance for this event, reduced performance would be expected for a snowfall event with stronger wind speeds which would further increase C_p . While the vector-based model acts to increase interception efficiency with wind speed, several studies suggest that canopy snow ablation increases as a result of wind induced unloading (Bartlett & Verseghy, 2015; Betts & Ball, 1997; Lumbrago et al., 2022; Roesch et al., 2001; Wheeler, 1987). While these studies have been used to develop parameterizations for wind induced unloading, they were not based on direct measurements of canopy snow unloading and further research is required to better refine these relationships to understand how wind influences canopy snow unloading after it is intercepted. Once the vector-based model is combined with a wind-induced canopy snow unloading parameterization, the overall influence of wind on canopy snow interception will be balanced to some extent.

Conclusions

New observations of snow interception, collected over a wide range of meteorological conditions and canopy structures suggest forest structure is the primary factor governing subcanopy snow accumulation. These findings challenge the theoretical foundation of most existing snow interception parameterizations, which rely on canopy snow load and air temperature as key predictors. At the point scale, high-temporal resolution measurements revealed no evidence of a maximum canopy snow load, even for snowfalls up to 45 kg m^{-2} , nor was there any indication of increased cohesion or branch bending affecting interception efficiency through air temperature. Instead, wind speed was found to either increase or decrease interception efficiency due to its influence on hydrometeor trajectory angle, which alters the apparent forest structure, or snow-leaf contact area.

At the forest plot scale, UAV-lidar measurements of throughfall collected over a wind-driven snowfall event confirmed the results observed at the point-scale and showed leaf contact area was the main factor governing the interception efficiency at a particular site. Canopy structure metrics adjusted for trajectory angle provided an improved predictor of interception efficiency compared to nadir canopy coverage. Plot-wide canopy structure was shown to be highly sensitive to simulated hydrometeor trajectory angles. For example, using VoxRS measurements snow-leaf contact area was observed to double for simulated hydrometeor trajectories associated with a wind speeds of 1 m s^{-1} compared to vertical hydrometeor trajectories. An existing theoretical relationship failed to represent the VoxRS measured increase in leaf contact area with simulated trajectory angles.

The lack of a strong association between air temperature or canopy snow load with interception efficiency, along with the clear influence of wind speed, underscores the need for a new snow interception parameterization. A new parameterization is proposed that calculates initial interception, prior to canopy snow ablation, as a function of snowfall and leaf contact area. This parameterization is consistent with many rainfall interception studies, which also separate canopy loading and ablation processes and calculate interception as a function of canopy coverage. Additionally, a second equation is proposed to estimate the increase in leaf contact area from nadir canopy coverage as a function of hydrometeor trajectory angle. This updated snow interception parameterization showed good performance in the subalpine forest in this study, but further validation should be conducted in a range of climates, forest species, and canopy structures. Caution is advised when applying this updated routine with existing canopy snow ablation parameterizations, as these were developed in conjunction with earlier snow interception routines that also incorporated ablation processes.

Acknowledgments

We wish to acknowledge financial support from the University of Saskatchewan Dean's Scholarship, Natural Sciences and Engineering Research Council of Canada, Global Water Futures Programme, Alberta Innovates and the Canada Research Chairs Programme. We thank Madison Harasyn, Hannah Koslowsky, Kieran Lehan, Lindsey Langs and Fortress Mountain Resort for their help in the field. Madison Harasyn, Alistair Wallace, and Rob White contributed to developing the UAV-lidar processing workflow.

Data Availability

The authors declare there are no competing interests.

References

- Axelsson, P. (2000). DEM Generation from laser scanner data using adaptive TIN models. *International Archives of the Photogrammetry, Remote Sensing and Spatial Information Sciences - ISPRS Archives*, 33, 110–117.
- Bartlett, P. A., & Verseghy, D. L. (2015). Modified treatment of intercepted snow improves the simulated forest albedo in the Canadian Land Surface Scheme. *Hydrological Processes*, 29(14), 3208–3226. <https://doi.org/10.1002/HYP.10431>
- BayesMap Solutions. (2024). *BayesStripAlign*. <https://bayesmap.com/products/bayesstripalign/>
- Betts, A. K., & Ball, J. H. (1997). Albedo over the boreal forest. *Journal of Geophysical Research: Atmospheres*, 102(D24), 28901–28909. <https://doi.org/10.1029/96JD03876>
- Calder, I. R. (1990). *Evaporation in the uplands*. Wiley.
- Cebulski, A., & Pomeroy, J. W. (2024). The theoretical underpinnings of snow interception and ablation parameterizations. *Wiley Interdisciplinary Reviews: Water, In Review*.
- Chianucci, F., & Macek, M. (2023). hemispheR: an R package for fisheye canopy image analysis. *Agricultural and Forest Meteorology*. <https://doi.org/10.1016/j.agrformet.2023.109470>
- Cionco, R. M. (1965). A Mathematical Model for Air Flow in a Vegetative Canopy. *Journal of Applied Meteorology* (1962), 4(4), 517–522. [https://doi.org/10.1175/1520-0450\(1965\)004%3C0517:AMMFAF%3E2.0.CO;2](https://doi.org/10.1175/1520-0450(1965)004%3C0517:AMMFAF%3E2.0.CO;2)
- Clark, M. P., Wood, A., Nijssen, B., Bennett, A., Knoben, W., & Lumbrazo, C. (2020). *SUMMA v3.0.3*. Zenodo. <https://doi.org/10.5281/zenodo.4558054>
- Dai, Y., Yuan, H., Xin, Q., Wang, D., Shangguan, W., Zhang, S., Liu, S., & Wei, N. (2019). Different representations of canopy structure—A large source of uncertainty in global land surface modeling. *Agricultural and Forest Meteorology*, 269–270(135), 119–135. <https://doi.org/10.1016/j.agrformet.2019.02.006>
- Deems, J. S., Painter, T. H., & Finnegan, D. C. (2013). Lidar measurement of snow depth: A review. *Journal of Glaciology*, 59(215), 467–479. <https://doi.org/10.3189/2013JoG12J154>
- Ellis, C. R., Pomeroy, J. W., & Link, T. E. (2013). Modeling increases in snowmelt yield and desynchronization resulting from forest gap-thinning treatments in a northern mountain headwater basin. *Water Resources Research*, 49(2), 936–949. <https://doi.org/10.1002/wrcr.20089>
- Essery, R., Pomeroy, J. W., Parviainen, J., & Storck, P. (2003). Sublimation of snow from coniferous forests in a climate model. *Journal of Climate*, 16(11), 1855–1864. [https://doi.org/10.1175/1520-0442\(2003\)016%3C1855:SOSFCF%3E2.0.CO;2](https://doi.org/10.1175/1520-0442(2003)016%3C1855:SOSFCF%3E2.0.CO;2)
- Floyd, W. C. (2012). *Snowmelt energy flux recovery during rain-on-snow in regenerating forests* [PhD Thesis]. August, 180.
- Floyd, W., & Weiler, M. (2008). Measuring snow accumulation and ablation dynamics during rain-on-snow events: innovative measurement techniques. *Hydrological Processes*, 22(24), 4805–4812.

- Fryer, G. I., & Johnson, E. A. (1988). Reconstructing Fire Behaviour and Effects in a Subalpine Forest. *The Journal of Applied Ecology*, 25(3), 1063–1072.
- Gelfan, A. N., Pomeroy, J. W., & Kuchment, L. S. (2004). Modeling forest cover influences on snow accumulation, sublimation, and melt. *Journal of Hydrometeorology*, 5(5), 785–803. [https://doi.org/10.1175/1525-7541\(2004\)005%3C0785:MFCIOS%3E2.0.CO;2](https://doi.org/10.1175/1525-7541(2004)005%3C0785:MFCIOS%3E2.0.CO;2)
- Golding, D. L., & Swanson, R. H. (1978). Snow accumulation and melt in small forest openings in Alberta. *Canadian Journal of Forest Research*, 8(4), 380–388. <https://doi.org/10.1139/x78-057>
- Harder, P., & Pomeroy, J. W. (2013). Estimating precipitation phase using a psychrometric energy balance method. *Hydrological Processes*, 27(13), 1901–1914. <https://doi.org/10.1002/hyp.9799>
- Harder, P., Pomeroy, J. W., & Helgason, W. D. (2020). Improving sub-canopy snow depth mapping with unmanned aerial vehicles: Lidar versus structure-from-motion techniques. *Cryosphere*, 14(6), 1919–1935. <https://doi.org/10.5194/tc-14-1919-2020>
- Harpold, A. A., Krogh, S. A., Kohler, M., Eckberg, D., Greenberg, J., Sterle, G., & Broxton, P. D. (2020). Increasing the efficacy of forest thinning for snow using high-resolution modeling: A proof of concept in the Lake Tahoe Basin, California, USA. *Ecohydrology*, 13(4). <https://doi.org/10.1002/eco.2203>
- Hedstrom, N. R., & Pomeroy, J. W. (1998). Measurements and modelling of snow interception in the boreal forest. *Hydrological Processes*, 12(10-11), 1611–1625. [https://doi.org/10.1002/\(SICI\)1099-1085\(199808/09\)12:10/11%3C1611::AID-HYP684%3E3.0.CO;2-4](https://doi.org/10.1002/(SICI)1099-1085(199808/09)12:10/11%3C1611::AID-HYP684%3E3.0.CO;2-4)
- Herwitz, S. R., & Slye, R. E. (1995). Three-dimensional modeling of canopy tree interception of wind-driven rainfall. *Journal of Hydrology*, 168(1-4), 205–226. [https://doi.org/10.1016/0022-1694\(94\)02643-P](https://doi.org/10.1016/0022-1694(94)02643-P)
- Hijmans, R. J. (2024). *terra: Spatial Data Analysis*. <https://cran.r-project.org/package=terra>
- Katsushima, T., Kato, A., Aiura, H., Nanko, K., Suzuki, S., Takeuchi, Y., & Murakami, S. (2023). Modelling of snow interception on a Japanese cedar canopy based on weighing tree experiment in a warm winter region. *Hydrological Processes*, 37(6), 1–16. <https://doi.org/10.1002/hyp.14922>
- Kim, E., Gatebe, C., Hall, D., Newlin, J., Misakonis, A., Elder, K., Marshall, H. P., Hiemstra, C., Brucker, L., De Marco, E., Crawford, C., Kang, D. H., & Entin, J. (2017). NASA's snowex campaign: Observing seasonal snow in a forested environment. *2017 IEEE International Geoscience and Remote Sensing Symposium (IGARSS)*, 1388–1390. <https://doi.org/10.1109/IGARSS.2017.8127222>
- Kozak, A., & Kozak, R. A. (1995). Notes on regression through the origin. *Forestry Chronicle*, 71(3), 326–330.
- Langs, L. E., Petrone, R. M., & Pomeroy, J. W. (2020). A $\delta^{18}\text{O}$ and $\delta^2\text{H}$ stable water isotope analysis of subalpine forest water sources under seasonal and hydrological stress in the Canadian Rocky Mountains. *Hydrological Processes*, 34(26), 5642–5658. <https://doi.org/10.1002/hyp.13986>
- LAStools. (2024). *Efficient LiDAR Processing Software (version 240220, academic)*. <http://rapidlasso.com/LAStools>
- Lehtonen, I., Kämärainen, M., Gregow, H., Venäläinen, A., & Peltola, H. (2016). Heavy snow

- loads in Finnish forests respond regionally asymmetrically to projected climate change. *Natural Hazards and Earth System Sciences*, 16(10), 2259–2271. <https://doi.org/10.5194/nhess-16-2259-2016>
- Lumbrazo, C., Bennett, A., Currier, W. R., Nijssen, B., & Lundquist, J. (2022). Evaluating Multiple Canopy-Snow Unloading Parameterizations in SUMMA With Time-Lapse Photography Characterized by Citizen Scientists. *Water Resources Research*, 58(6), 1–22. <https://doi.org/10.1029/2021WR030852>
- Lundberg, A. (1993). Evaporation of intercepted snow — Review of existing and new measurement methods. *Journal of Hydrology*, 151(2), 267–290. [https://doi.org/10.1016/0022-1694\(93\)90239-6](https://doi.org/10.1016/0022-1694(93)90239-6)
- Lundberg, A., & Hallidin, S. (1994). Evaporation of intercepted snow: Analysis of governing factors. *Water Resources Research*, 30(9), 2587–2598. <https://doi.org/10.1029/94WR00873>
- Lundquist, J. D., Dickerson-Lange, S., Gutmann, E., Jonas, T., Lumbrazo, C., & Reynolds, D. (2021). Snow interception modelling: Isolated observations have led to many land surface models lacking appropriate temperature sensitivities. *Hydrological Processes*, 35(7), 1–20. <https://doi.org/10.1002/hyp.14274>
- Mahat, V., & Tarboton, D. G. (2014). Representation of canopy snow interception, unloading and melt in a parsimonious snowmelt model. *Hydrological Processes*, 28(26), 6320–6336. <https://doi.org/10.1002/hyp.10116>
- Moeser, D., Stähli, M., & Jonas, T. (2015). Improved snow interception modeling using canopy parameters derived from airborne LiDAR data. *Water Resources Research*, 51(7), 5041–5059. <https://doi.org/10.1002/2014WR016724>
- Musselman, K. N., Pomeroy, J. W., & Link, T. E. (2015). Variability in shortwave irradiance caused by forest gaps: Measurements, modelling, and implications for snow energetics. *Agricultural and Forest Meteorology*, 207, 69–82. <https://doi.org/10.1016/j.agrformet.2015.03.014>
- Natural Resources Canada. (2024). *Precise point positioning*. <https://webapp.csrs-scrs.nrcan-rncan.gc.ca/geod/tools-outils/ppp.php>
- Niu, G. Y., & Yang, Z. L. (2004). Effects of vegetation canopy processes on snow surface energy and mass balances. *Journal of Geophysical Research D: Atmospheres*, 109(23), 1–15. <https://doi.org/10.1029/2004JD004884>
- Nock, C. A., Lecigne, B., Taugourdeau, O., Greene, D. F., Dauzat, J., Delagrange, S., & Messier, C. (2016). Linking ice accretion and crown structure: towards a model of the effect of freezing rain on tree canopies. *Annals of Botany*, 117(7), 1163–1173.
- Pomeroy, J. W., Fang, X., & Ellis, C. R. (2012). Sensitivity of snowmelt hydrology in Marmot Creek, Alberta, to forest cover disturbance. *Hydrological Processes*, 26(12), 1891–1904. <https://doi.org/10.1002/hyp.9248>
- Pomeroy, J. W., & Gray, D. M. (1995). *Snowcover Accumulation, Relocation and Management* (NHRI Scien, p. 144). National Hydrology Research Institute, Environment Canada, Saskatoon, Canada.
- Pomeroy, J. W., Marsh, P., & Gray, D. M. (1997). Application of a distributed blowing snow model to the arctic. *Hydrological Processes*, 11(11), 1451–1464. <https://doi.org/10.1002/>

- (sici)1099-1085(199709)11:11%3C1451::aid-hyp449%3E3.0.co;2-q
- Pomeroy, J. W., Parviaainen, J., Hedstrom, N., & Gray, D. M. (1998). Coupled modelling of forest snow interception and sublimation. *Hydrological Processes*, 12(15), 2317–2337. [https://doi.org/10.1002/\(SICI\)1099-1085\(199812\)12:15%3C2317::AID-HYP799%3E3.0.CO;2-X](https://doi.org/10.1002/(SICI)1099-1085(199812)12:15%3C2317::AID-HYP799%3E3.0.CO;2-X)
- R Core Team. (2024). *R: A Language and Environment for Statistical Computing*. R Foundation for Statistical Computing. <https://www.r-project.org/>
- Rittger, K., Raleigh, M. S., Dozier, J., Hill, A. F., Lutz, J. A., & Painter, T. H. (2020). Canopy Adjustment and Improved Cloud Detection for Remotely Sensed Snow Cover Mapping. *Water Resources Research*, 56(6), n/a. <https://doi.org/10.1029/2019WR024914>
- Roesch, A., Wild, M., Gilgen, H., & Ohmura, A. (2001). A new snow cover fraction parameterization for the ECHAM4 GCM. *Climate Dynamics*, 17(12), 933–946. <https://doi.org/10.1007/s003820100153>
- Safa, H., Krogh, S. A., Greenberg, J., Kostadinov, T. S., & Harpold, A. A. (2021). Unraveling the Controls on Snow Disappearance in Montane Conifer Forests Using Multi-Site Lidar. *Water Resources Research*, 57(12), 1–20. <https://doi.org/10.1029/2020WR027522>
- Satterlund, D. R., & Haupt, H. F. (1967). Snow catch by Conifer Crowns. *Water Resources Research*, 3(4), 1035–1039. <https://doi.org/10.1029/WR003i004p01035>
- Schmidt, R. A., & Gluns, D. R. (1991). Snowfall interception on branches of three conifer species. *Canadian Journal of Forest Research*, 21(8), 1262–1269. <https://doi.org/10.1139/x91-176>
- Schmidt, R. A., & Troendle, C. A. (1989). Snowfall into a forest and clearing. *Journal of Hydrology*, 110(3-4), 335–348. [https://doi.org/10.1016/0022-1694\(89\)90196-0](https://doi.org/10.1016/0022-1694(89)90196-0)
- Smith, C. D. (2007). Correcting the wind bias in snowfall measurements made with a Geonor T-200B precipitation gauge and alter wind shield. *87th AMS Annual Meeting*.
- Staines, J., & Pomeroy, J. W. (2023). Influence of forest canopy structure and wind flow on patterns of sub-canopy snow accumulation in montane needleleaf forests. *Hydrological Processes*, 37(10), 1–19. <https://doi.org/10.1002/hyp.15005>
- Storck, P., Lettenmaier, D. P., & Bolton, S. M. (2002). Measurement of snow interception and canopy effects on snow accumulation and melt in a mountainous maritime climate, Oregon, United States. *Water Resources Research*, 38(11), 1–16. <https://doi.org/10.1029/2002wr001281>
- Troendle, C. A. (1983). The Potential for Water Yield Augmentation From Forest Management in the Rocky Mountain Region. *Journal of the American Water Resources Association*, 19(3), 359–373. <https://doi.org/10.1111/j.1752-1688.1983.tb04593.x>
- Valante, F., David, J. S., & Gash, J. H. C. (1997). Modelling interception loss for two sparse eucalypt and pine forests in central Portugal using reformulated Rutter and Gash analytical models. *Journal of Hydrology*, 190(1-2), 141–162. [https://doi.org/10.1016/S0022-1694\(96\)03066-1](https://doi.org/10.1016/S0022-1694(96)03066-1)
- Van Stan, J. T., Siegert, C. M., Levia, D. F., & Scheick, C. E. (2011). Effects of wind-driven rainfall on stemflow generation between codominant tree species with differing crown characteristics. *Agricultural and Forest Meteorology*, 151(9), 1277–1286. <https://doi.org/10.1016/j.agrformet.2011.05.008>
- Varhola, A., Coops, N. C., Weiler, M., & Moore, R. D. (2010). Forest canopy effects on

- snow accumulation and ablation: An integrative review of empirical results. *Journal of Hydrology*, 392(3-4), 219–233. <https://doi.org/10.1016/j.jhydrol.2010.08.009>
- Verseghy, D. L. (2017). *Class – The Canadian Land Surface Scheme (version 3.6.1) technical documentation*. (January; p. 174). Environment; Climate Change Canada Internal Rep. https://zenodo.org/record/6562376/files/Verseghy_2017_CLASSv3.6.1_Documentaton.pdf
- Vionnet, V., Mortimer, C., Brady, M., Arnal, L., & Brown, R. (2021). Canadian historical Snow Water Equivalent dataset (CanSWE, 1928–2020). *Earth System Science Data*, 13(9), 4603–4619.
- Wheater, H. S., Pomeroy, J. W., Pietroniro, A., Davison, B., Elshamy, M., Yassin, F., Rokaya, P., Fayad, A., Tesemma, Z., Princz, D., Loukili, Y., DeBeer, C. M., Ireson, A. M., Razavi, S., Lindenschmidt, K., Elshorbagy, A., MacDonald, M., Abdelhamed, M., Haghnegahdar, A., & Bahrami, A. (2022). Advances in modelling large river basins in cold regions with Modélisation Environnementale Communautaire—Surface and Hydrology (MESH), the Canadian hydrological land surface scheme. *Hydrological Processes*, 36(4), 1–24.
- Wheeler, K. (1987). *Interception and redistribution of snow in a subalpine forest on a storm-by-storm basis*. Western Snow Conference. <http://sites/westernsnowconference.org/PDFs/1987Wheeler.pdf>

Supporting Information

Detailed Description of UAV-Lidar Methodology

The REIGL miniVUX-2 laser operates at a near infrared wavelength with a laser beam footprint of 0.160 m x 0.05 mm (at 100 m above ground). The accuracy and precision of the miniVUX-2 is described by REIGL for a lab environment of 0.015 m and 0.01 m respectively (at 50 m above ground). The miniVUX-2 was configured with a laser pulse repetition rate of 200 kHz, field of view of 360°, scan speed of 31.09 revolutions s⁻¹ and an angular step width of 0.0558°, resulting in an expected average point cloud density of 107 returns m⁻² for each flight path.

Georeferenced point clouds with x, y, and z coordinates for each laser return were generated following methods outlined by Harder et al. (2020) and Staines & Pomeroy (2023) to reconcile survey lidar, IMU and GNSS data. A ground-based GNSS system was positioned on a permanent monument during each survey and underwent precise point positioning (PPP) correction by Natural Resources Canada (2024). Differential GNSS correction of the UAV trajectory was conducted using the ground-based PPP GNSS observations and the POSPac UAV software. The UAV-lidar point clouds were then transformed from a sensor referenced coordinate system to a georeferenced coordinate system (EPSG:32611 - WGS 84 / UTM zone 11N) using the RIEGL Riprocess Software. A vertical offset of up to 6 cm between UAV-lidar flight lines was observed in the resulting point clouds on March 13th and 14th, 2024 and was attributed to IMU position drift. This offset between flight lines was corrected using the BayesStripAlign

software v2.24 (BayesMap Solutions, 2024), which reduces relative and absolute uncertainties in the vertical elevation of the point cloud using the ground control points (GCP) collected across the study site using a differential GNSS rover.

Quality control, ground classification and calculation of the change in between two UAV-lidar point clouds was conducted using the LAStools software package (LAStools, 2024). The ground classification was conducted using the “lasground_new” function (LAStools, 2024) for both the pre and post snowfall event point clouds, with a step size set to 2 m and 8 substeps (ultra_fine setting). The offset and spike options were set to remove points that are more than 0.1 m above or below the initial ground surface estimate surface which “lasground_new” fits to the last returns. This function is based on an algorithm outlined by Axelsson (2000), describing the process of making the initial ground surface element.

The change in elevation between the two UAV-lidar surveys was interpreted as the increase in snow accumulation, ΔHS over the snowfall event. This change was calculated using a point-to-grid subtraction method, using the “lasheight” function from the LAStools (2024) software, as in Deems et al. (2013) and Staines & Pomeroy (2023). The pre snowfall event point cloud from “lasground_new” by “lasheight” to construct a “ground” TIN. Subsequently, the height of each post snowfall event point above the ground TIN, resulting in a point cloud representing ΔHS . This point cloud was then converted into a raster of ΔHS with a grid cell resolution of 5 x 5 cm using the “las2dem” function. Further quality control and resampling of the 5 cm raster of ΔHS was conducted using the ‘Terra’ R package (Hijmans, 2024). Areas that were disturbed over the snowfall event during the in-situ snow survey and values that exceeded the .999th quantile were removed. To help remove any remaining noise a 25 cm ΔHS raster was generated by computing the median of the 5 cm ΔHS values within each 25 cm grid cell.

Linear Regression Models Through the Origin

Kozak & Kozak (1995) noted, the default R^2 value provided for least squares models forced through the origin by many statistical packages can be misleading. Therefore, these R^2 values were adjusted using Equation 10 in Kozak & Kozak (1995) and two statistical tests as described by Kozak & Kozak (1995) were used to verify whether a no-intercept model (forced through the origin) was appropriate for this data compared to a with-intercept model. The first test evaluated if the intercept of the with-intercept was significantly different from zero using p-value provided by the ‘summary’ function from the ‘stats’ package in R (R Core Team, 2024). The second test examined if there was a significant difference between the no-intercept and with-intercept models by testing if the residual sum of squares was different between the no-intercept and full model, assessed via Equation 15 in Kozak & Kozak (1995). If the first test indicated a significant difference, and the second did not, the no-intercept model could be deemed statistically justified (Kozak & Kozak, 1995).